Copy No. _____

Defence Research and Development Canada
Recherche et développement pour la défense Canada

DEFENCE R&D DÉFENSE

Modeling Gas Bubble Behaviour and Loading on a Rigid Target due to Close-Proximity Underwater Explosions

Comparison to Tests Conducted at DRDC Suffield

Mark Riley

Defence R&D Canada – Atlantic

Technical Memorandum
DRDC Atlantic TM 2010-238
November 2010

Canada

This page intentionally left blank.

Modeling Gas Bubble Behaviour and Loading on a Rigid Target due to Close-Proximity Underwater Explosions

Comparison to Tests Conducted at DRDC Suffield

Mark Riley

Defence R&D Canada – Atlantic

Technical Memorandum
DRDC Atlantic TM 2010-238
November 2010

Principal Author

Original signed by Mark Riley

Mark Riley

Defence Scientist WP

Approved by

Original signed by Neil Pegg

Neil Pegg

Section Head WP

Approved for release by

Original signed by Ron Kuwahara for

Calvin Hyatt

DRP Chair

Abstract

This study describes recent simulation results for underwater explosions in close-proximity to a rigid target. Simulations were performed using Chinook, an Eulerian computational fluid dynamics (CFD) code. Predicted fluid pressures, impulse loading on the target, gas bubble size and bubble collapse times are compared with measurements taken from a series of experiments and compared to empirical models. The experiments, which were conducted at DRDC Suffield as part of the Force Protection TDP in 2008, involved 1.1 g detonator charges and 40 g C4 charges detonated at standoff distances ranging from 0.2 up to 2.0 times the free-field bubble radius from a rigid target. At these ranges of standoff distance, both the shock wave and gas bubble make significant contributions to the loading on the target surface.

The simulations of the rigid target tests primarily focused on the modelling of gas bubble collapse and water jetting behaviour. Both two-dimensional and three-dimensional simulations were performed. Chinook was found to qualitatively predict the general trends correctly, however quantitative gaps still exist. From the high speed experimental videos and the animation of the numerical simulations it was found that the maximum impulse due to a bubble collapse occurs for the largest standoff in which the bubble contacts the target before collapse. The results were found to be very mesh dependent, and refining the mesh did not always produce better agreement with experiments. This was observed most often in the bubble collapse impulse loading. The two-dimensional approach provided a good initial understanding of the physical behaviour for a limited computational effort, and produced better bubble periods when compared to experimental data. The three-dimensional simulations were found to produce improved impulse predictions for the rigid targets.

Résumé

La présente étude décrit des résultats d'explosions sous-marines près d'une cible rigide simulées récemment. Les simulations ont été effectuées à l'aide de Chinook, un logiciel qui utilise la dynamique numérique des fluides et un résolveur à intervalles de temps explicites (méthode Euler). Les pressions de liquide prévues, la pression exercée sur la cible par l'impulsion, la taille des bulles de gaz et les temps d'effondrement des bulles sont comparés aux mesures tirées d'une série d'expériences et aux modèles empiriques. Les expériences, qui ont été réalisées à RDDC Suffield dans le cadre du projet de démonstration de technologies de protection de la Force maritime en 2008, impliquaient des charges à détonateur de 1,1 g et des charges de C4 de 40 g que l'on a fait exploser à une distance de sécurité, variant entre 0,2 et 2,0 fois le rayon de bulle de type champ libre, d'une cible rigide. À cette distance de sécurité, l'onde de choc et la bulle de gaz contribuent de façon significative à la pression exercée à la surface de la cible.

Les simulations des essais sur cible rigide se concentraient principalement sur la modélisation de l'effondrement des bulles de gaz et sur la formation des jets d'eau. Des simulations en deux dimensions et des simulations en trois dimensions ont été effectuées. On a découvert que le Chinook prédit de façon qualitative les tendances générales correctement bien qu'il y ait encore des failles au niveau quantitatif. À partir des vidéos expérimentaux à haute vitesse et de

l’animation des simulations numériques, on a découvert que l’impulsion maximale due à l’effondrement d’une bulle se produit pour la plus importante distance dans laquelle la bulle touche à la cible avant effondrement. On a découvert que les résultats dépendaient beaucoup du maillage; de plus, le fait de raffiner le maillage ne produisait pas toujours une plus grande conformité aux résultats expérimentaux. Cela a été observé la plupart du temps dans la pression d’impulsion d’effondrement de bulle. L’approche à deux dimensions a fourni une bonne compréhension initiale du comportement physique contre un effort d’analyse limité, et a produit de meilleures périodes de bulle que les données expérimentales. On a découvert que les simulations en trois dimensions produisent des prédictions d’impulsion améliorées pour les cibles rigides.

Executive summary

Modeling Gas Bubble Behaviour and Loading on a Rigid Target due to Close-Proximity Underwater Explosions: Comparison to Tests Conducted at DRDC Suffield

Mark Riley; DRDC Atlantic TM 2010-238; Defence R&D Canada – Atlantic; November 2010.

Introduction: Ship vulnerability to underwater explosion loading is being investigated as part of the Maritime Force Protection (MFP) TDP. The ultimate goal of this project is to deliver a validated capability to predict these types of loading which can then be applied to full scale ships. This study is aimed at developing the capability to accurately model the loading on rigid targets subjected to close proximity underwater explosions. Numerical simulations were performed to predict the loading due to the bubble collapses for a series of close- proximity underwater explosion configurations ranging from 0.2 up to 2.0 times the maximum free-field bubble radius.

Results: This report provides the results of a study using the computational fluids dynamic code Chinook to model the loading on a rigid plate caused by close proximity underwater explosions. Different models were developed to determine the accuracy of each approach in comparison with experimental results, including two-dimensional and three-dimensional models. The bubble collapse impulse was predicted within 20 percent for the three-dimensional models, with over half the predictions being within 10 percent of the experiments. The coarse two-dimensional models were generally within 20-25 percent of the experiments. The refined two-dimensional models showed larger discrepancies when compared to the experiments. For all models the first bubble collapse peak pressures and second bubble collapse loadings were significantly over-predicted by the numerical simulations when compared to the experiments.

Significance: Currently there are few analysis tools for predicting the loading due to the bubble collapse events that occur during close proximity underwater explosions. The findings of this study show that Chinook has the capability to model the full loading regime on rigid targets due to close proximity underwater explosions with acceptable accuracy. The findings of this study also show that two-dimensional models, which could be effective for full scale ship structures, can be used to obtain acceptable preliminary predictions of the loading on a system with limited computational requirements.

Future plans: Improvements to Chinook are planned. These improvements will help with the bubble collapse functionality as well as the issues with the divergence of the two-dimensional analyses.

Sommaire

Modeling Gas Bubble Behaviour and Loading on a Rigid Target due to Close-Proximity Underwater Explosions: Comparison to Tests Conducted at DRDC Suffield

Mark Riley; DRDC Atlantic TM 2010-238; R & D pour la défense Canada – Atlantique; Novembre 2010.

Introduction : La vulnérabilité des navires aux pressions exercées par les explosions sous-marines est étudiée dans le cadre du projet de démonstration de technologies de protection de la Force maritime. Le but ultime de ce projet est de produire une technique validée permettant de prédire ces types de pressions, et que l'on peut ensuite appliquer aux navires grandeur nature. La présente étude vise à développer la capacité de modéliser avec précision les pressions exercées sur les cibles rigides soumises à des explosions sous-marines à proximité. Des simulations numériques ont été réalisées afin de prédire la pression produite par l'effondrement des bulles pour une série de configurations d'explosion sous-marine à proximité allant de 0,2 à 2,0 fois le rayon de bulle de type champ libre maximal.

Résultats : Le présent rapport donne les résultats d'une étude utilisant le logiciel qui utilise la dynamique numérique des fluides et nommé Chinook pour modéliser la pression exercée sur une plaque rigide et produite par des explosions sous-marines à proximité. Différents modèles ont été développés pour déterminer la précision de chaque approche par rapport aux résultats expérimentaux, y compris les modèles à deux dimensions et les modèles à trois dimensions. La pression d'effondrement des bulles a été prédite à 20 % près pour les modèles à trois dimensions, plus de la moitié des prédictions étant à 10 % près des résultats expérimentaux. Les modèles à deux dimensions grossiers étaient en général à 20-25 % près des résultats expérimentaux. Les modèles à deux dimensions raffinés présentaient des écarts plus grands lorsque comparés aux résultats expérimentaux. Pour tous les modèles, les pressions maximales d'effondrement de première bulle et les pressions d'effondrement de deuxième bulle prédites par les simulations numériques étaient beaucoup trop grandes lorsque comparées aux résultats expérimentaux.

Portée : Présentement, il y a peu d'outils d'analyse permettant de prédire la pression produite par l'effondrement des bulles qui se produit lors d'explosions sous-marines à proximité. Les conclusions de la présente étude démontrent que le Chinook est en mesure de modéliser, avec une précision acceptable, toutes les pressions qui sont exercées sur des cibles rigides suite à des explosions sous-marines à proximité. La présente étude démontre aussi que les modèles à deux dimensions, qui pourraient être efficaces pour les structures de navire grandeur nature, peuvent être utilisés pour obtenir des prédictions

préliminaires acceptables de la pression à l'aide d'un système ayant des capacités d'analyse limitées.

Recherches futures : Les améliorations à apporter au Chinook sont planifiées. Ces améliorations seront utiles pour la fonctionnalité d'effondrement des bulles, ainsi que pour les problèmes concernant la divergence des analyses à deux dimensions.

This page intentionally left blank.

Table of contents

List of figures

List of tables

Acknowledgements

The author would like to acknowledge Julian Lee from DRDC Suffield for permitting the use of the experimental results.

1 Introduction

Naval vessels can be subjected to severe blast loading from both air and underwater explosions. In the case of air blasts the loading mechanisms are well understood and can be modeled with reasonable accuracy with currently available numerical analysis tools such as LS-DYNA [1] and Chinook [2]. However, for underwater explosions in close proximity to a structure, the loading mechanism is entirely different. With underwater explosions, a shock is formed that propagates through the water and loads the structure with a significant pressure pulse. An underwater explosion will also generate a pulsating gas bubble whose size depends on the chemical composition of the explosive, the mass of the charge, and the depth of the charge in the water. When the charge is detonated within a distance of twice the maximum free-field bubble radius, R, from the structure, the bubble collapse and the water jet that is created by the collapse are very likely to be directed at the structure. At even closer ranges the bubble collapses directly onto the structure resulting in loading that can be more severe than the shock loading. The bubble will then reform and pulsate against the structure resulting in more loading cycles. During the bubble collapse the boundary of the bubble farthest from the structure typically collapses through the center of the bubble, allowing a water jet directed toward the structure to form and causing the bubble to change from a spherical to toroidal shape as shown in Figure 1.

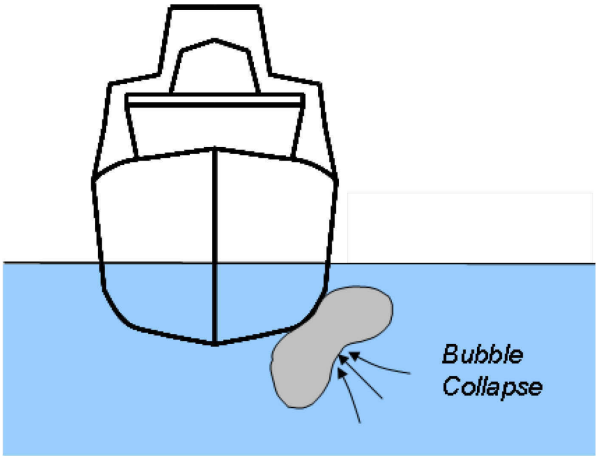

Figure 1: Bubble collapse and water jet formation against a structure

As part of the Maritime Force Protection (MFP) TDP, ship vulnerability to underwater explosion loading is being investigated. The ultimate goal of this project is to deliver a validated capability to predict these types of loading which can then be applied to full scale ships. This study is aimed at developing the capability to accurately model the loading on rigid targets subjected to close proximity underwater explosions. As part of

the MFP TDP, underwater explosion experiments are being conducted at DRDC Suffield on rigid and deformable targets.

In this report results are provided for an extensive numerical analysis study using two-dimensional and three-dimensional models of the explosion process. The accuracy and efficiency of each modeling approach is compared. The shock and bubble collapse pressure and impulse loadings and the arrival time of the first two bubble collapses are compared to the experimental results. The gas bubble maximum radius and period are also compared to free-field empirical models.

2 Experimental investigation

The rigid target experiments used for this study were conducted at DRDC Suffield in 2008. The rigid target was placed on a concrete block at the bottom of the pond which measured 3.5 ft x 3.5 ft x 3 ft high.

2.1 Test Pond and Target Plate

The test pond, shown in Figure 2, is a truncated cone shape with a surface diameter of 50 m, a bottom diameter of 16 m and a depth of 8 m.

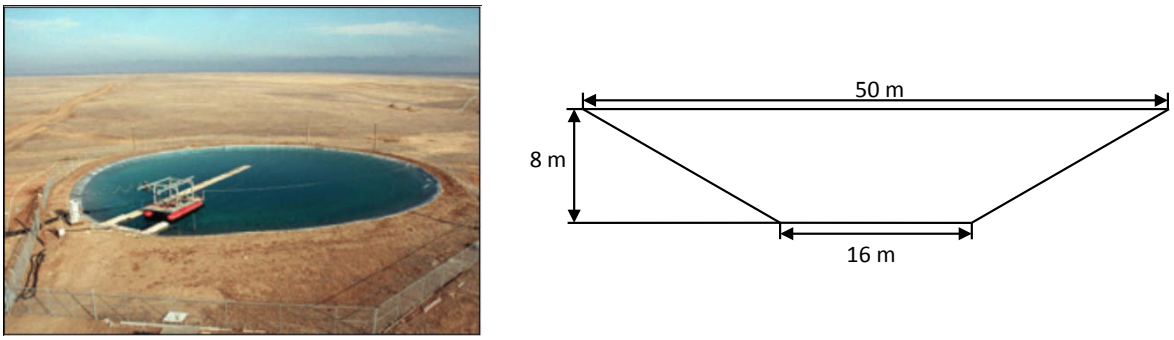

(a) (b)

Figure 2: Test pond facility at DRDC Suffield (a) Picture (b) Schematic of front view

The rigid plate was positioned at the bottom of the basin on a concrete block. The concrete block was positioned at the center of the pond and measured 44 in × 44 in × 36 in. The depth of the water above the plate surface was measured to be approximately 6 m at the time of the experiments. The target plate, shown in Figure 3, is 914 mm in diameter and 76 mm thick.

Figure 3: Target plate used for the rigid plate experiments conducted at DRDC Suffield

2.2 Instrumentation

The plate was instrumented with 7 embedded pressure gauges, two free field gauges away from the target, and two gauges taped to the surface of the target plate. The embedded gauges were positioned as shown in Table 1, where the radius is measured from the center of the target plate. The location of the free-field and target surface gauges varied with the standoff of the charge. The embedded gauges were mounted within cavities in the plate, as shown in Figure 4, which was a technique developed to withstand the shock loading from the explosion as well as the fluid flow from the bubble expansion and collapse without a significant loss of gauges. This technique is not expected to provide the appropriate levels for the shock loading; however the main focus of this study was the bubble collapse loading. The types of gauges were Neptune Sonar TR2-5000G piezoelectric pressure gauges.

Table 1: Pressure measurement gauges embedded in the rigid plate close proximity UNDEX experiments at DRDC Suffield

Gauge ID	Gauge Type	Manufacturer	Radius (mm)
C01	TR2-500G in cavity	Neptune Sonar	0
C02	TR2-500G in cavity	Neptune Sonar	5
C03	TR2-500G in cavity	Neptune Sonar	10
C04	TR2-500G in cavity	Neptune Sonar	15
C05	TR2-500G in cavity	Neptune Sonar	20
C06	TR2-500G in cavity	Neptune Sonar	25
C07	TR2-500G in cavity	Neptune Sonar	50

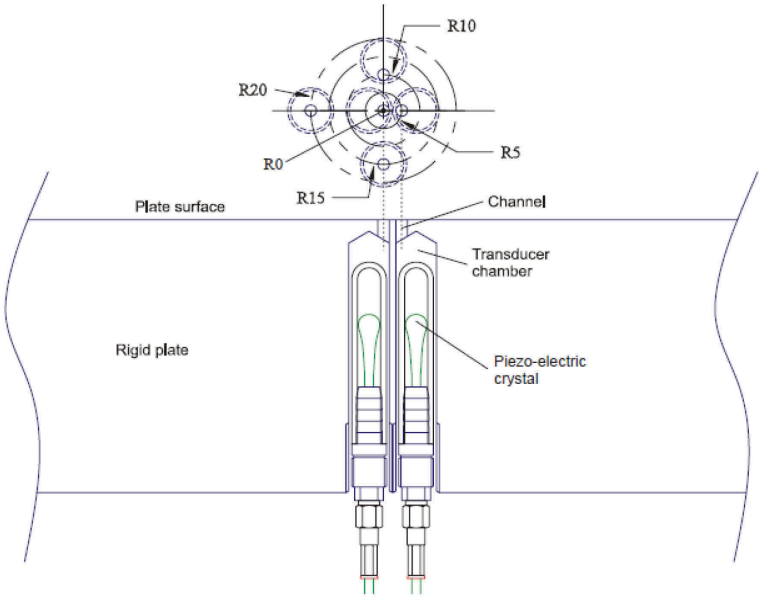

Figure 4: Gauge embedding technique for Suffield rigid plate experiments

From the pressure time histories recorded by the embedded gauges the gas bubble period was determined as the time to the peak pressure in each of the bubble collapse events. The impulse of the loading (i.e. impulse jump due to the individual loading events) was determined by numerically integrating the pressure time history over the duration of the individual loading events. The pressure measurements from the free field gauges were used to compare shock pressures.

2.3 Test Series

The series of experiments conducted on the rigid plate are as shown in Table 2. The standoff distance was modified throughout the series of experiments for the 1.1g detonator charge, with a single standoff for the 40 g C4 charge. Numerical simulations were performed for all test cases.

Table 2: Test Set-up for rigid plate experiments conducted at DRDC Suffield

Test	Charge Size (g)	Standoff (R)	Test	Charge Size (g)	Standoff (R)
P08262C	1.1	0.20	P08260D	1.1	0.93
P08262H	1.1	0.20	P08260C	1.1	1.00
P08262B	1.1	0.35	P08262D	1.1	1.00
P08262A	1.1	0.50	P08262E	1.1	1.00
P08261F	1.1	0.60	P08262F	1.1	1.10
P08261E	1.1	0.65	P08262G	1.1	1.25
P08261D	1.1	0.70	P08260B	1.1	1.50
P08261C	1.1	0.76	P08260A	1.1	2.00
P08261B	1.1	0.80	P08273A	40	0.60
P08261A	1.1	0.85	P08276A	40	0.60

3 Empirical Models

3.1 Similitude Equations

The peak pressure and decay of the primary shock wave follow the form of the following similitude equations, where K_i and A_i are constants based on the type of charge and unit system used.

$$P_{\max} = K_1 \left(\frac{W^{1/3}}{R} \right)^{A_1} \tag{1}$$

$$I = K_3 W^{1/3} \left(\frac{W^{1/3}}{R} \right)^{A_3} \tag{2}$$

$$\theta = K_2 W^{1/3} \left(\frac{W^{1/3}}{R} \right)^{A_2} \tag{3}$$

where P_{max} is the peak pressure in psi, θ is the decay constant in ms, W the charge weight in pounds of explosive and R the standoff in feet. Similarly, the maximum bubble radius is estimated from:

$$R_{b\max} = K_6 \left(\frac{W}{D+33} \right)^{1/3} \tag{4}$$

where R_{bmax} is the maximum bubble radius in feet and D is the charge depth in feet. The bubble period T_b in s is estimated by:

$$T_b = K_5 \frac{W^{1/3}}{(D+33)^{5/6}} \tag{5}$$

The volume of the gas bubble can be reasonably approximated by a half sine function according to Eq. (6), where V_o is the initial charge volume and V_{max} is the maximum bubble volume calculated with the maximum bubble radius, given by Eq. (4), assuming a spherical bubble.

$$V(t) = V_o + (V_{\max} - V_o) \cdot \sin\left(\frac{\pi t}{T_b}\right) \tag{6}$$

From the volume time relation of the bubble the radius time history can be determined by Eq. (7), assuming a spherical gas bubble.

$$R(t) = \left(\frac{3}{4\pi} V(t)\right)^{1/3} \tag{7}$$

The similitude constants for the charge materials used in this study are shown in Table 3.

Table 3: Similitude constants for the RP-83 detonator and C4 explosives based on the imperial unit system [3]

Constant	RP-83	C4
K_1	31.6×10^3	24.7×10^3
K_2	0.0403	56.57
K_3	1.442	1.461
K_5	4.615	4.545
K_6	14.01	13.86
A_1	1.150	1.240
A_2	-0.211	-0.239
A_3	0.912	0.924

Since the similitude expressions do not account for any energy loss in the bubble radius or period, an energy loss function proposed by TNO [4] is applied to the charge weight at the time of minimum bubble radii. The energy loss expression is as shown in Eq. (8).

$$\lambda = 0.2575 + (1 - 0.2575)\exp(-0.8148m) \tag{8}$$

where m is the bubble cycle number such that the first bubble cycle after detonation has the values $m = 0$ and $\lambda = 1$. At the first bubble minimum, m becomes 1, λ equals 0.5862, and the charge weight becomes λW. The weight is substituted into Eqs. (4) and (5) to determine the maximum gas bubble radius and bubble period for the next cycle. This process is repeated at the subsequent bubble minimums.

4 Numerical Simulations

The numerical modelling for this study was conducted using Chinook, a computational fluid dynamics code developed by Martec Ltd [2] specifically designed for modeling explosions, and which is based on the Euler inviscid fluid dynamics equations (i.e. conservation of mass, momentum, and energy). In the present study the target plate is nearly rigid so simulations were conducted using Chinook with a fixed boundary with similar geometry as the target plate.

4.1 Material Modeling

In Chinook simulations, equations of states (EOS) are used to define pressure as a function of density for each of the materials. The Jones-Wilkens-Lee (JWL) EOS was used for the Composition A and Composition 4, C4, explosive materials, the Tait EOS for the water, and the ideal gas EOS for the air. The material properties and EOS constants used for the fluids are shown in Table 3. The properties for the C4 were provided by FOI, whereas the properties used for water and air is generally accepted values.

Table 4: Equation of state properties for the Chinook Analyses

JWL parameters			Tait parameters for Water		Ideal gas parameters for air	
	C4	Comp. A				
A (Pa)	609.8×10^9	611.3×10^9	Pressure (Pa)	93000	γ	1.4
B (Pa)	12.95×10^9	10.65×10^9	Density (kg/m^3)	1000	Density (kg/m^3)	1.177
C (Pa)	1.804×10^9	1.804×10^9	B	3000	Molar Weight	28.97
R1	4.50	4.40	N	7.14	Spec Energy (J/kg)	2.15×10^5
R2	1.40	1.20	M	5.000		
ω	0.25	0.32	Spec Energy (J/kg)	3.54×10^5		
Spec Energy (J/kg)	5.625×10^6	5.394×10^6				

4.2 Modeling Approach

Several different analyses were performed for a 1.1 g Composition A detonator charge at standoffs ranging from 0.2R up to 2.0R as well as a 40 g C4 charge at a standoff of 0.6R. These include analyses using two-dimensional and three-dimensional models with various mesh densities. For all analyses the initial shock propagation phase of the loading was mapped from refined two-dimensional analyses onto the coarser meshes for the full time analyses. A more detailed discussion of the models used is provided in the following sections.

4.2.1 Two-Dimensional Mesh Development

With a rigid target plate there is no requirement to model the target deformation and therefore it is possible to model the three-dimensional problem in two-dimensions. An underwater explosion in the free-field is axisymmetric about the vertical axis and can be adequately modelled in two-dimensions. For explosions in a confined fluid region, such as a pond, an axisymmetric approach is valid provided the basin and target geometry are axisymmetric. For these experiments this was the case.

Several two-dimensional models were created to simulate the experimental cases. Figure 5 shows the general domain shape and the coarse mesh used for the two-dimensional models. The inverted cone shape of the test pond at Suffield was made to reduce the influence of the reflected pressure waves on the test specimen, and is not modeled in the numerical simulations. A very coarse mesh at the outer limits is implemented which will smear the high pressure waves and make any reflection from the square side walls in the model negligible. In Figure 5 (b) the red area is the water, the blue is air, and because no boundary tracker is present in Chinook, the light blue and yellow bands at the water/air interface are regions where the density of the water and air are averaged based on volume of each material in cells adjacent to the interface.

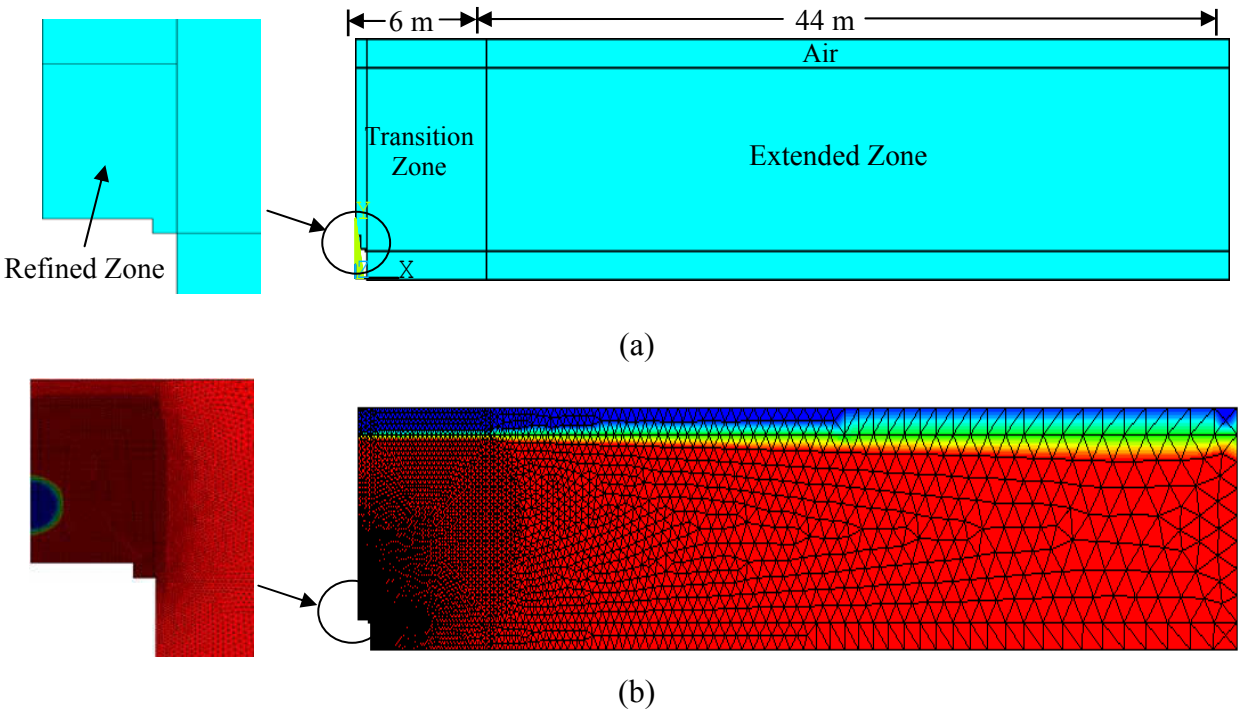

Figure 5: Two-dimensional domain used to model the DRDC Suffield UNDEX test pond (a) Geometric domain (b) Example coarse mesh

All two-dimensional meshes were created using triangular cells. Triangular cells allow for the formation of a better bubble shape when compared to square cells. Numerous two-dimensional models were created with varying degrees of refinement. Table 4 shows the mesh densities used for the various two-dimensional models, where R1 and R2 refer to refined models of progressively increasing degree of refinement. The models were created by first creating a geometric model of the basin cross section in ANSYS [5]. The geometric model was split at the material interfaces to ensure a row of nodes existed at the interface, which limits the degree of density averaging in the elements at the boundary (i.e. the light blue and yellow bands in Figure 5(b)). The meshes were generated by defining the cell size on each of the area boundaries and creating a free mesh. The edges that have graded meshes were assigned a cell size according to the length of the edge and the size of the cells required at the two ends. The number of cells ranged from 41228 for the coarse meshes to 389232 cells for the R2 meshes.

Table 5: Refined zone size and mesh densities used for two-dimensional analyses

Simulation Case	Refined zone dimensions		Refined zone cell size (mm)			Transition zone cell size	Extended zone cell size
	height (mm)	width (mm)	C	R1	R2		
All models	800	558.8	7	3.5	1.75	Gradually increased up to 200 mm at the outer boundaries	Gradually increased up to 850 mm at the outer boundaries

4.2.2 Three-Dimensional Mesh Development

All three-dimensional models used quarter models with symmetry planes added on the cut surfaces. Similar to the full time two-dimensional models the mapping method was used such that a uniform fluid mesh was used throughout the volume where the bubble would form, (i.e. the refined zone). Figure 6 shows the geometric model used for creating the mesh for the three-dimensional analyses. Similar to the two-dimensional analyses the models were created using the ANSYS [5] pre-processor. Using a code developed in house the ANSYS mesh was converted to LS-DYNA format. The code Dyna2Chinook, an executable provided by Martec Ltd. with Chinook, was then used to convert the LS-DYNA mesh into the Chinook mesh.

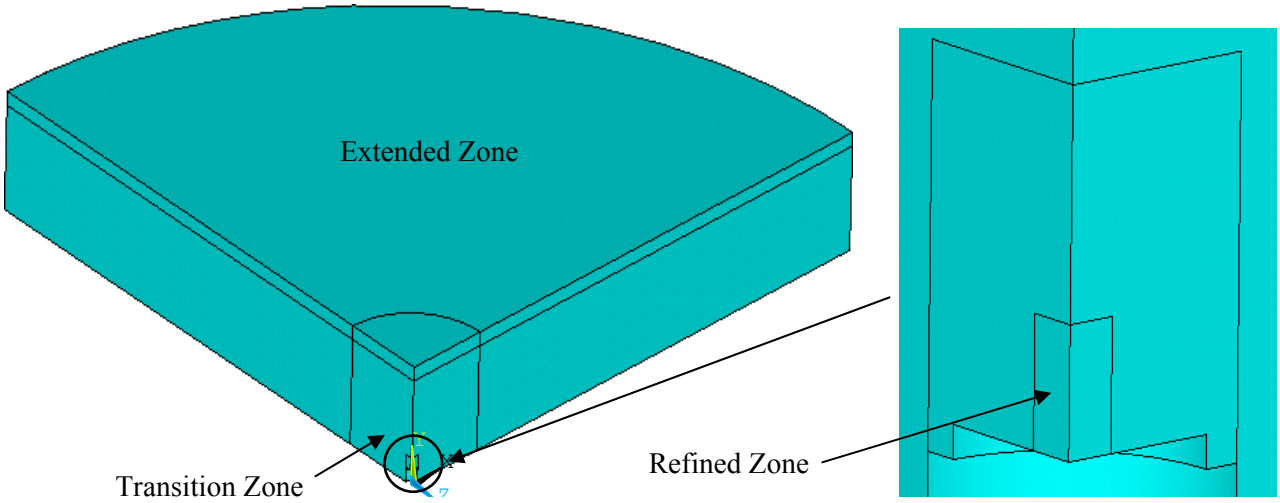

Figure 6: Three-dimensional geometric domain used to model the DRDC Suffield UNDEX test pond

The mesh density in the refined zone was 7 mm or 10 mm depending on the experiment that was being simulated. For all standoffs having the 1.1 g detonator charge a 7 mm mesh was used for the refined region. For standoffs between 1.0R and 1.5R a mesh of 10 mm was also used in the refined zone to determine the effect of the coarser mesh. The dimensions of the refined zone were chosen to ensure they were larger than the maximum bubble radius. For the three-dimensional models tetrahedral elements were used for the cell shapes for the same reason that triangular elements were used for the two-dimensional meshes. The mesh densities for all the three-dimensional models are shown in Table 6.

Table 6: Refined zone dimensions and mesh densities for the three-dimensional models

Model	Refined zone dimensions		Refined zone cell size (mm)	Transition zone cell size (mm)	Extended zone cell size (mm)	Number of cells (x 100,000)
	height (mm)	width (mm)				
1.1 g at 0.2R to 1.0R	300	160	7	7-500	500-1000	6.76
1.1 g at 1.1R to 1.5R	370	160				7.24
1.1 g at 1.0R to 1.5R	370	160	10	10-500		4.49
1.1 g at 2.0R	460	160	7	7-500		9.15
40 g at 0.6R	824	560	10	10-500		9.04

4.3 Analysis Approach

Due to the time step size in Chinook being related to the size of the smallest cell in the model, a mapping approach was used to increase the analysis time step size and in turn decrease the analysis run time. Studies were conducted by Martec Ltd. on deformable targets, [6,7], which found that a refined two-dimensional analysis could be performed to propagate the shock front of the explosion to the target plate, and then map this onto a three-dimensional mesh for the bubble growth and collapse phases of the analysis. For rigid targets, the mapping from the two-dimensional model can be postponed until the shock front propagates beyond the target. A three-dimensional mesh refinement study was performed [7] and it was found that a mesh of 12mm was sufficient in the volume of the bubble formation to get comparable results to a three-dimensional analysis run from the start of the explosion, based on a charge size of 20 g C4. This was determined by comparing the final displacement of a deformable target analyzed using a mapped approach to experimental results.

In the present study a refined two-dimensional model was used to propagate the shock prior to mapping to the coarse two and three-dimensional models. The greater refinement of the two-dimensional models allows the propagating shock front to be more accurately defined. The shock propagation mesh was developed with triangular cells that had a minimum cell size of 1.0 mm for all the 1.1 g detonator charge standoffs and 2 mm for the 40 g C4 charge. For all analyses the shock propagation model was run until the shock front had passed by all the gauge locations, such that the full shock event, including the decay of the pressure pulse, had occurred at all gauge locations. A previous study [8] showed that mapping the shock onto a coarser mesh before it has impacted the plate can reduce the peak pressure up to 33 percent and the impulse up to approximately 4 percent.

The mapping to a two or three-dimensional model is performed by starting the analyses from restart files created by the shock propagation model. When the analysis is restarted the coarse mesh is initialized with the results from the refined model including pressure, fluid velocities, and densities. If the mapping is performed from a two-dimensional model to a three-dimensional model the two-dimensional domain is placed on its plane in the three-dimensional space and rotated about the vertical axis to initialize the entire 3D model domain. When the mapping is performed between models with the same dimensions, the model being mapped to will be initialized by the overlapping volumes. The coarse meshes are initialized by computing the average of the variables of the smaller cells that overlap the larger cell.

The Chinook simulations were run on DRDC Atlantic's SGI Altix 4700, 88 core cluster computer. The analyses were run using various numbers of processors, based on availability of the system. All the 1.1 g detonator charge three-dimensional models were run on 20 cores and had run times ranging from one to two days. The fastest runs were for the models with the 10 mm mesh in the refined region and the longest was for the 2.0R standoff with the 7 mm mesh in the refined region. The three dimensional model

for the 40 g C4 charge was run on 30 cores and had a run time of approximately 2.5 days. The main reason for the increase in the run time for the 40 g charge is that the analysis was run for duration of 150 ms, whereas for the 1.1 g charge they were only run up to 50 ms. The two dimensional models were analyzed using 10 cores and had run times ranging from 45 minutes for the coarse models with the 1.1 g detonator up to 3 days for the most refined model with the 40 g charge. With the intermediate mesh density, the two-dimensional models took 6 and 15 hours for the 1.1 g and 40 g charges respectively. These numbers show why it is beneficial to model in two-dimensions with coarser meshes.

To determine the capability of Chinook to model the free-field gas bubble size accurately, analyses were conducted for several standoffs implementing a two-dimensional mesh. These analyses assumed a standoff of 10 m from the target, with the same charge depth as the close-proximity analyses. For these analyses the mesh of the refined region was refined to 0.5 mm.

One feature that Chinook lacks in its analysis capabilities is a material interface tracking capability for determining the boundary between different fluids. Without this capability no definite boundary between the gas bubble and the water exists. Currently, the density is averaged in the cells that possess both the gas bubble and water. By not having clear delineation between gas and water, the loading produced by the collapse of the gas bubble is in some way averaged or smeared out. This is more prevalent after the first bubble collapse when there is a significant mixing region of combined water and gas instead of well defined water and gas regions. The first bubble maximum and second bubble maximum are shown in Figure 7, where the red color indicates water, dark blue is explosive gas, and other colors indicate a mixed region.

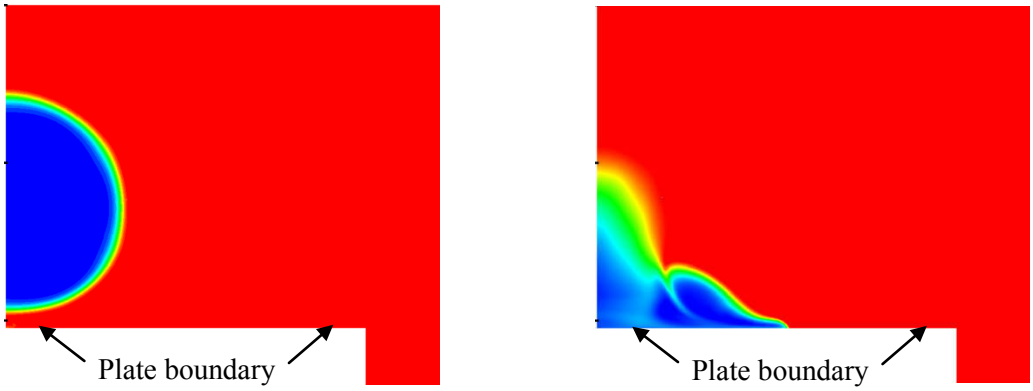

Figure 7: Bubble formation in the Chinook simulations (a) first bubble maximum (b) second bubble maximum

In order to determine the ability of Chinook to simulate the expansion and collapse of the explosive gas bubble several characteristics were observed in the simulations. These

include the gas bubble radius time histories, which were only saved for the coarser two-dimensional meshes to reduce file sizes, and the pressure time histories at the locations of the experimentally measured responses. Similar to the experimental results, the gas bubble period was taken as the time to the peak pressure in each of the bubble collapse events. The impulse of the loading (i.e. impulse jump due to the individual loading events) was determined by numerically integrating the pressure time history over the duration of the individual loading events.

5 Results

In order to determine the ability of Chinook to accurately model the bubble collapse event associated with close proximity UNDEX events, the results have been divided into two categories. The first is the ability of Chinook to model the dynamics of the gas bubble including formation and collapse. This includes comparing the simulation results of the maximum bubble radius and bubble collapse period to the experimental and similitude results when available. The second category looks at the capabilities of Chinook to simulate the loading on the structure. This includes comparing the shock and subsequent bubble collapse pressures and impulses to experimental and similitude results where applicable.

5.1 Gas Bubble Dynamics

5.1.1 Gas Bubble Radius

Examples of the gas bubble radius time histories for the free field similitude equations, Chinook simulations, Chinook free-field simulations, and experimental bubble periods are shown in Figure 8.

As these results show the first maximum bubble radius is under predicted by Chinook compared to the free field similitude equations. This would be expected as the free field similitude equations do not account for the interaction between the target and the bubble which would generally reduce the bubble radius, and prolong the bubble period. For the second gas bubble radius Chinook significantly under predicts the similitude response. Figure 8 shows the free-field Chinook results show good agreement with the free-field similitude maximum bubble radius for the first gas bubble maximum. Chinook predicts much smaller gas bubble radii for subsequent bubble cycles.

Figure 9 shows the maximum gas bubble radius for the 1.1g charge at various standoffs between 0.2R and 2.0R. Figure 9 shows that mesh refinement results in a slightly larger gas bubble radii. This is due to the boundary of the gas bubble exhibiting less diffusion for the refined models. For increasing standoffs the initial gas bubble radius slowly approaches the similitude value, which shows that the rigid target influences the gas bubble formation for the close proximity charges.

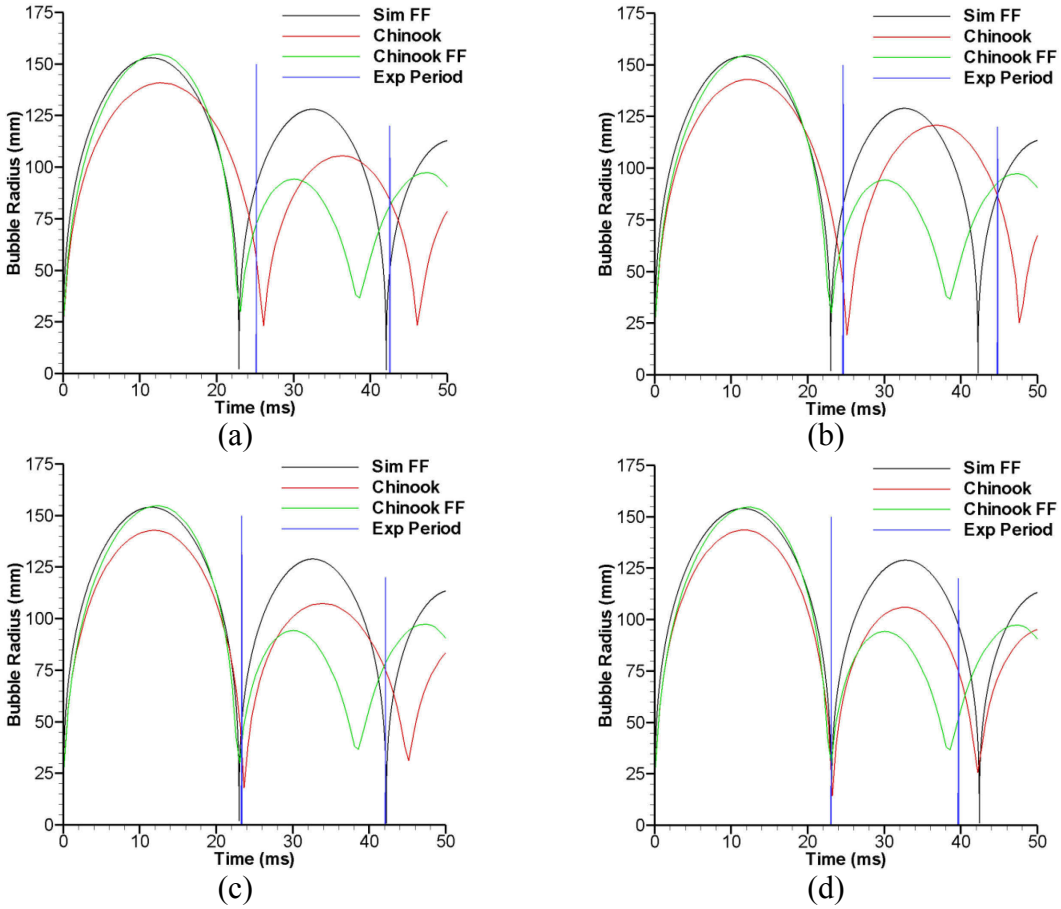

Figure 8: Gas bubble time histories (a) RP-83 detonator at 0.5R (b) RP-83 detonator at 1.0R (c) RP-83 detonator at 1.5R (d) RP-83 detonator at 2.0R (FF stands for free-field)

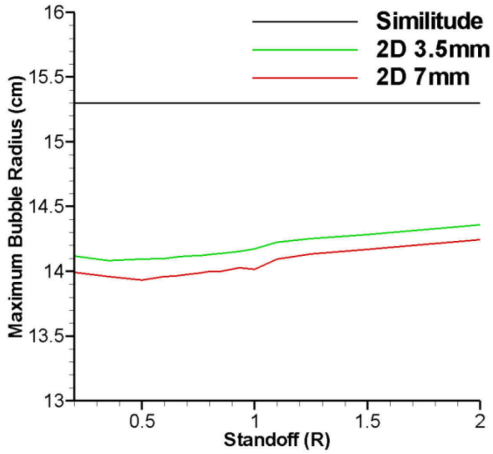

Figure 9: Maximum bubble radius versus the standoff for the 1.1g RP-83 detonator

5.1.2 Gas Bubble Period

Figure 10 shows the gas bubble period versus the standoff distance for various gauge locations. The numerical values of the bubble periods for all gauge locations are shown in Appendix A.

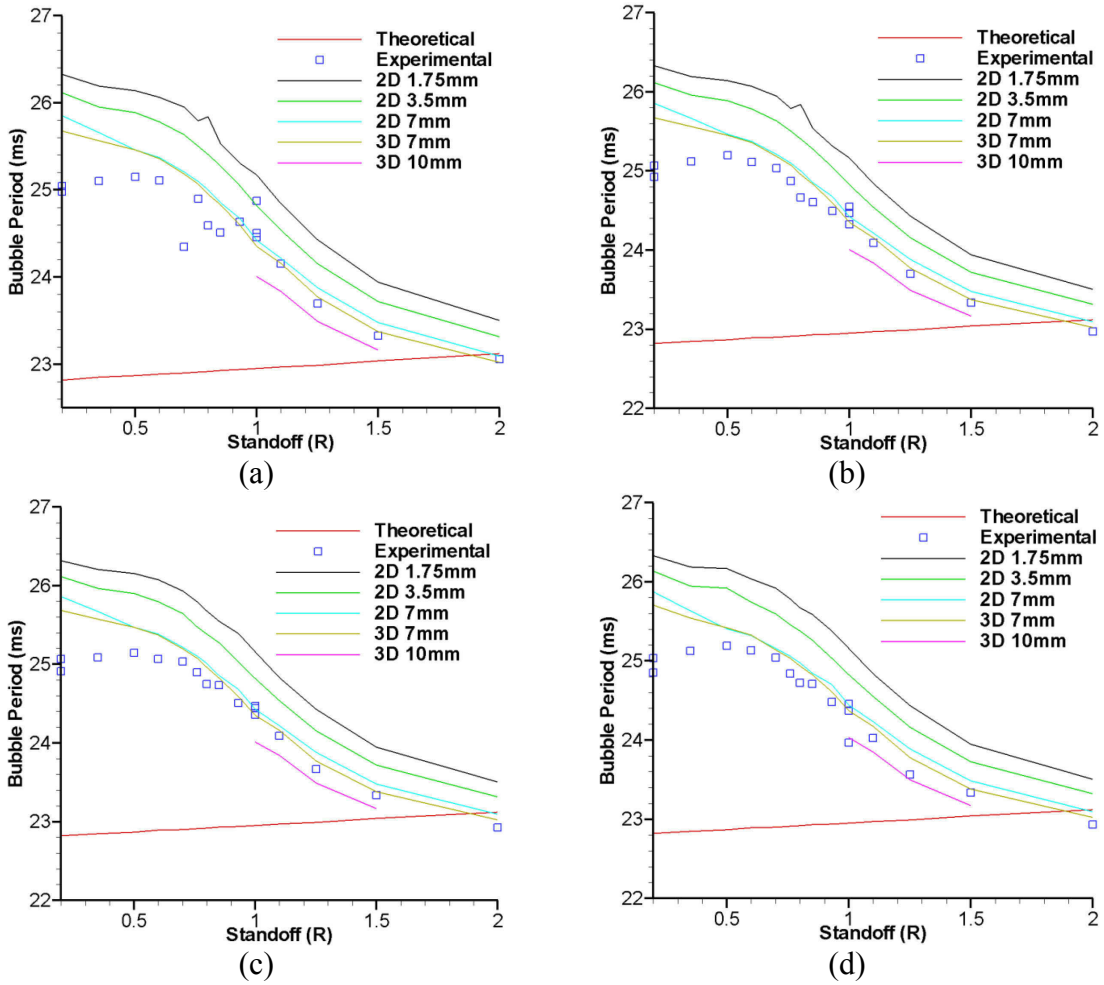

Figure 10: First gas bubble periods at the (a) 0mm gauge (b) 10mm gauge (c) 25mm gauge (d) 50mm gauge

From the experimental results it can be seen that the bubble period increases slightly as the charge is moved away from the target plate up to a standoff of 0.5R at which point the bubble period decreases with increasing standoff. The Chinook simulations predict the bubble period is a maximum at the closest standoff and decreases as the charge is moved further from the plate. As was seen in a previous study [8], with mesh refinement the bubble period increases and diverges from the experimental results for two-dimensional meshes. For standoffs over 0.5R, the three-dimensional and coarse two-dimensional simulations predict a bubble period very close to the experimental results.

Klaseboer et al. [9] had previously found that the bubble period in the presence of a structure was increased by 5-10 percent depending on the standoff. The results of this study also show that the first gas bubble period at small standoffs is 9 and 11 percent larger than the analytical free-field bubble period for the experimental and numerical results respectively. The numerical and experimental bubble periods approach the analytical value with an increasing standoff, with the three methods showing good agreement at a standoff of 2.0R.

Figure 11 shows the percent difference between the experimental and Chinook first bubble collapse arrival times.

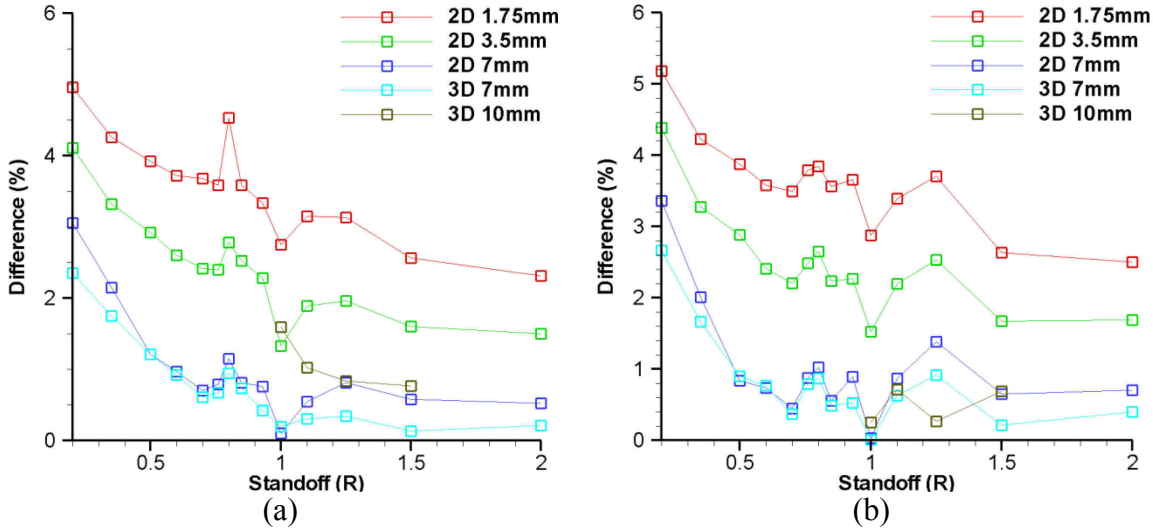

Figure 11: Percent difference between the experimental and Chinook first gas bubble collapse arrival time (a) 5 mm gauge (b) 50 mm gauge

Figure 12 and Figure 13 show the period and percent difference between the experimental and Chinook for the second gas bubble collapse.

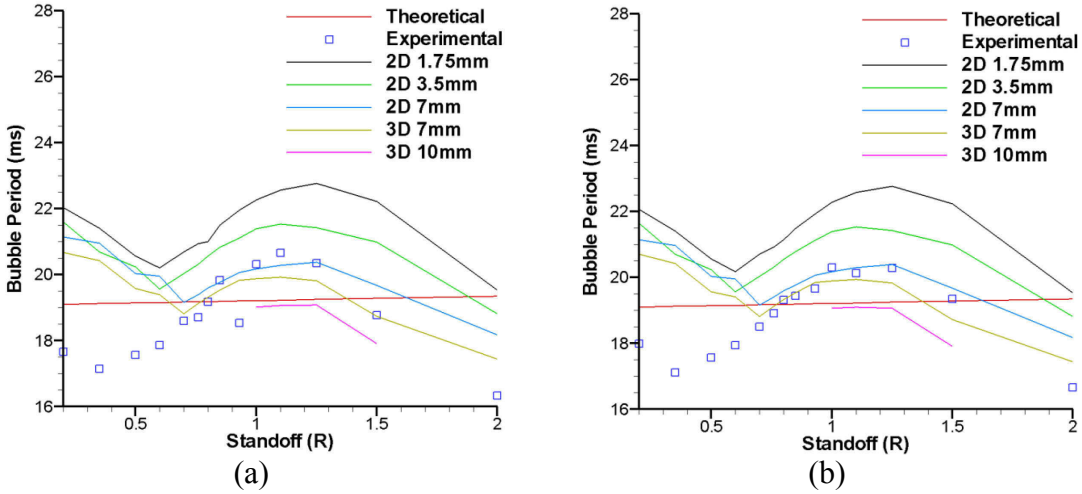

Figure 12: Second gas bubble period at the (a) 5mm gauge (b) 20mm gauge

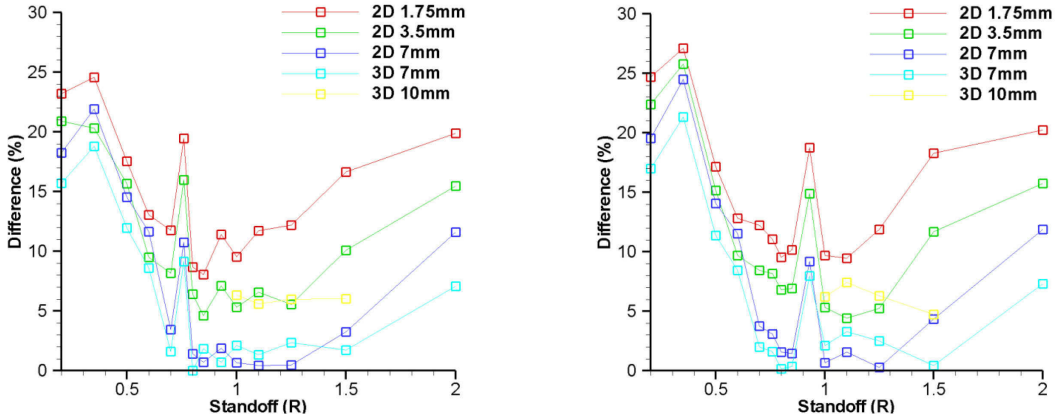

Figure 13: Percent difference between the experimental and Chinook second gas bubble collapse arrival time (a) 10 mm gauge (b) 25 mm gauge

Figure 12 and Figure 13 show Chinook can reasonably predict the second bubble collapse period for standoffs greater than 0.6R when compared to the experiments. There is excellent agreement between Chinook and experiments for standoffs between 0.7R and 1.5R. In general, over the range of standoffs, the three-dimensional 7mm mesh predicts the bubble collapse period closer to the experimental bubble period than the other models, with the coarse two-dimensional mesh producing similar results for standoffs between 0.7R and 1.5R.

5.2 Loading Comparisons

5.2.1 Peak Pressures

Example pressure time history plots for the shock, first bubble collapse, and second bubble collapse is shown in Figure 14 through Figure 16 respectively.

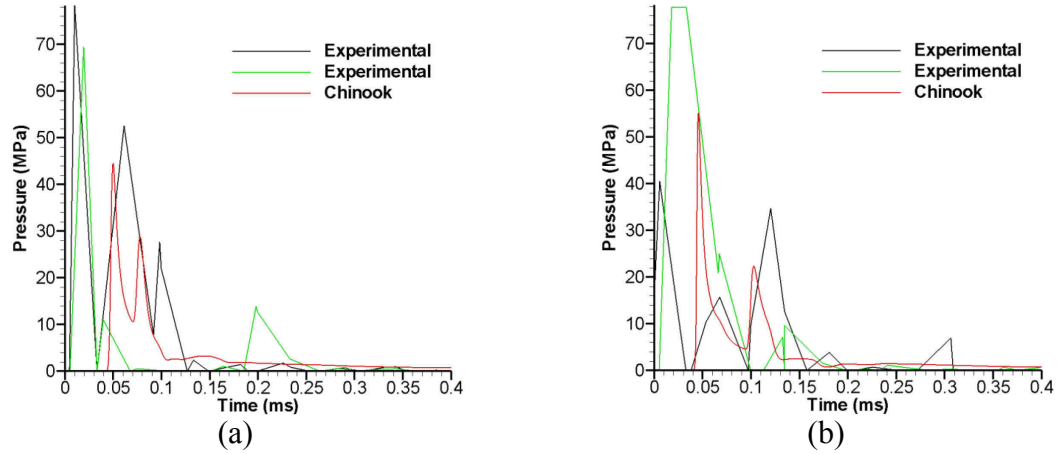

Figure 14: Shock pressure time history for the free field gauges for the 1.1 g detonator charge at standoffs of (a) 0.2R and (b) 0.5R

The time lag between the experimental and numerical predictions for the shock pressure time histories, Figure 14, is the time for the shock wave to reach the plate in the numerical simulations. For the experimental results, time zero was taken as the arrival time of the shock front, whereas for the simulations it was taken as the start time of the analysis. This time lag does not affect the bubble collapse periods as it is very small relative to the bubble collapse periods. In general the pressure predictions by Chinook are significantly less than the values measured at the free field gauges in the experiments.

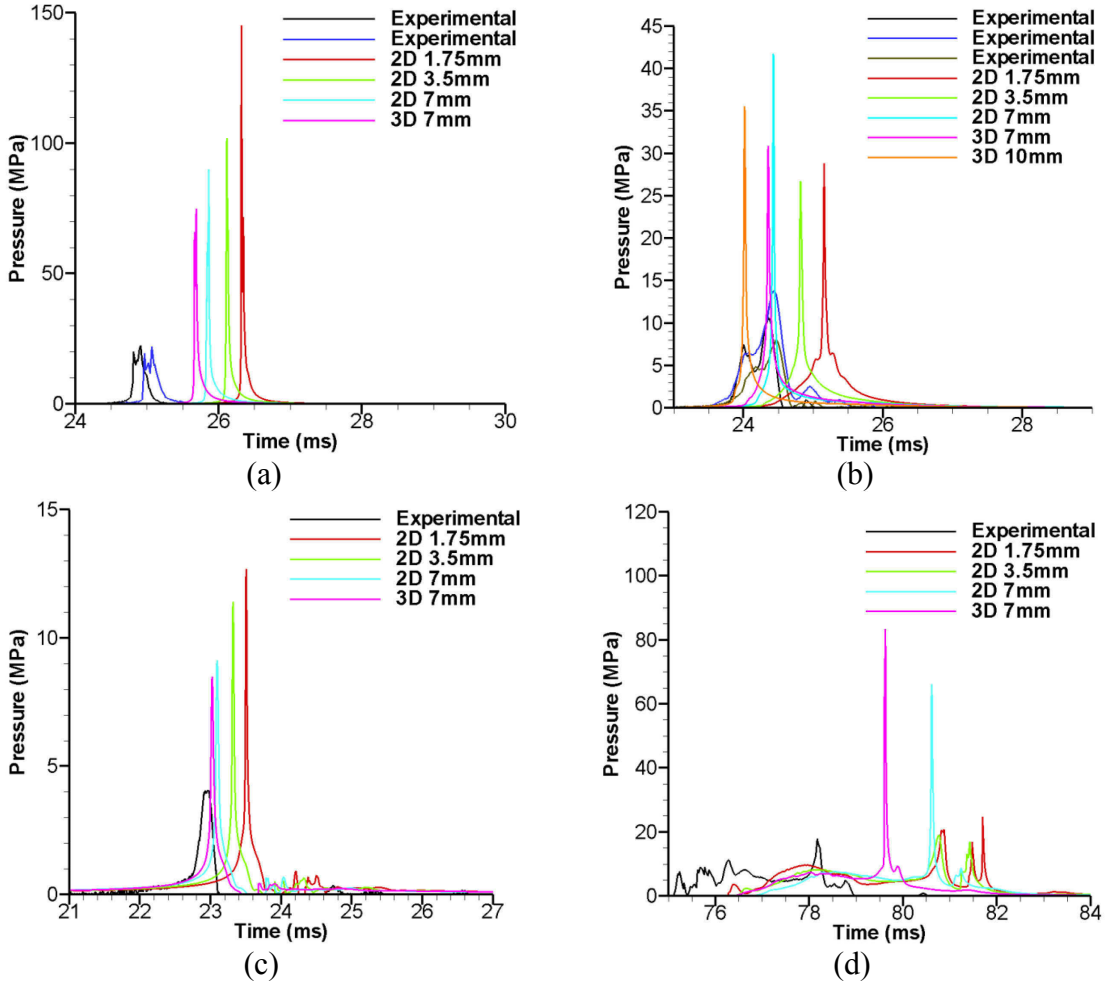

Figure 15: First bubble collapse pressure time history for the 25mm gauge at standoffs of (a) 1.1g RDX at 0.2R, (b) 1.1g RDX at 1.0R, (c) 1.1g RDX at 2.0R (d) 40g C4 at 0.6R

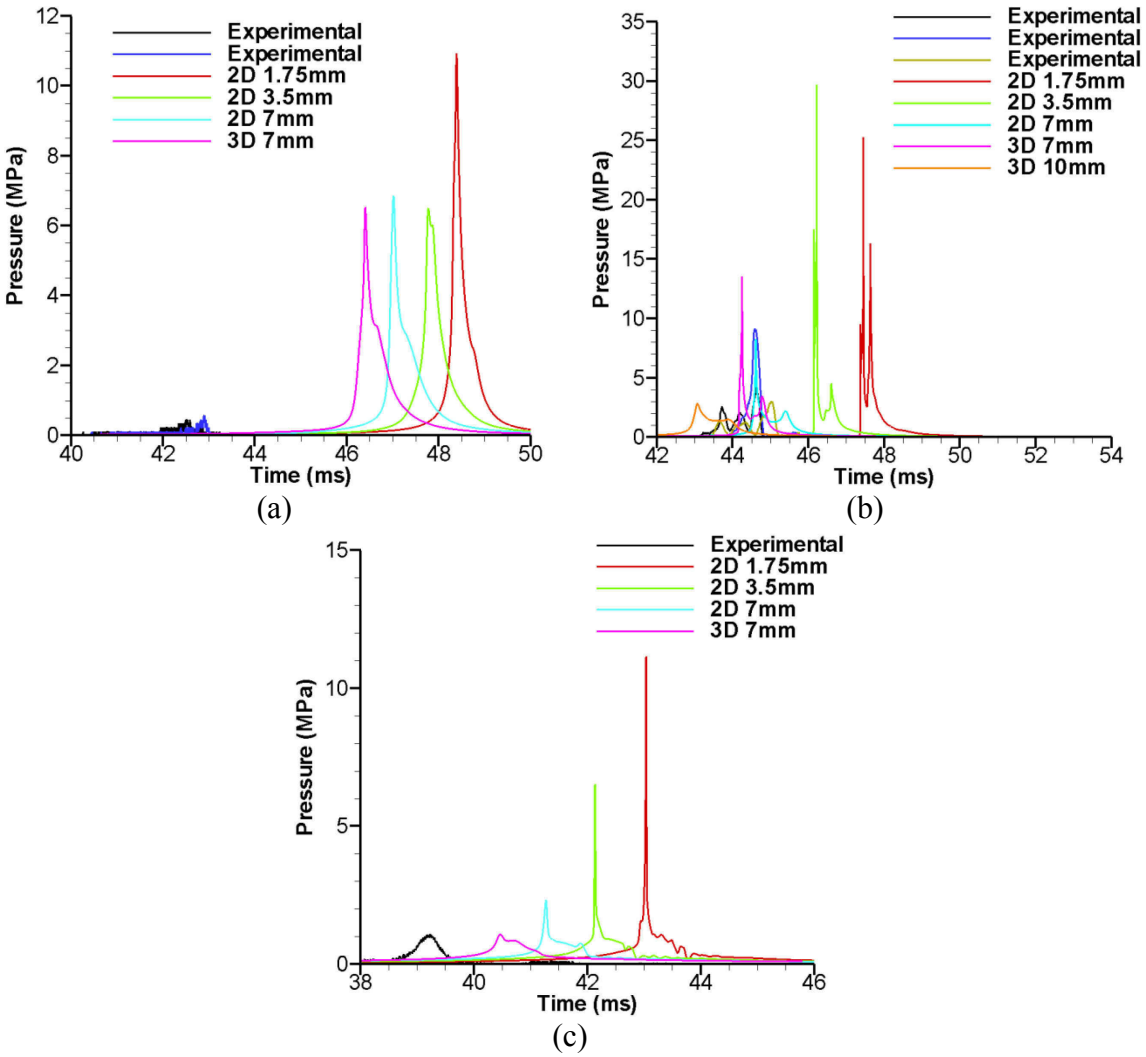

Figure 16: Second bubble collapse pressure time history for the 25mm gauge for the 1.1 g detonator charge at standoffs of (a) 0.2R, (b) 1.0R and (c) 2.0R

Figure 15 and Figure 16 show that the bubble collapse pressures are significantly over predicted by all Chinook models when compared to the experimental measurements. The level of over prediction by the models is reduced as the charge standoff is increased.

An example of the peak pressure versus standoff for the bubble collapse events at the 25 mm gauge is shown in Figure 17.

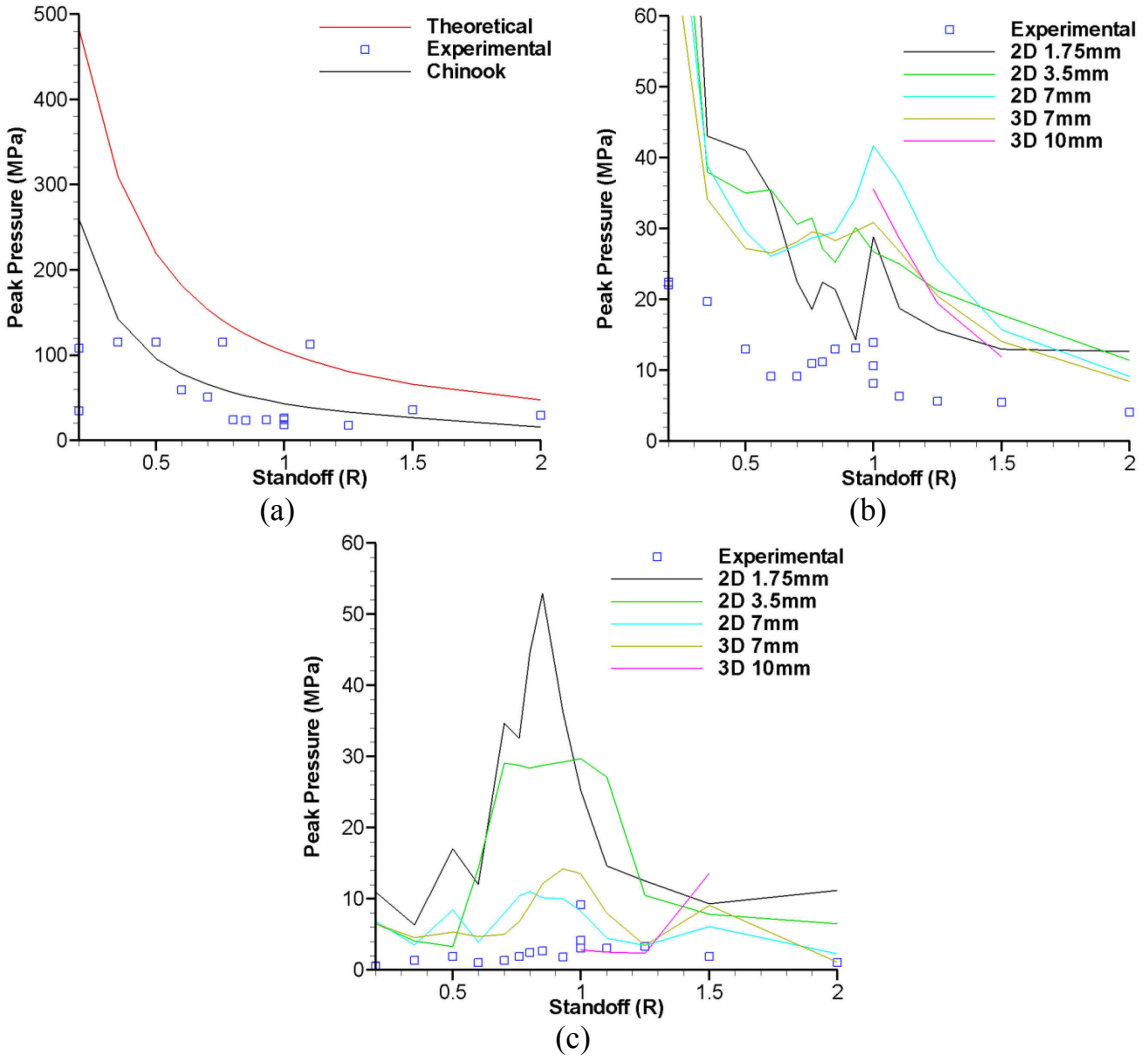

Figure 17: Comparison of the peak pressures as a function of standoff for the 1.1 g detonator charge at the 25 mm gauge location (a) Shock, (b) first bubble collapse, (c) second bubble collapse

From Figure 17(a) it can be seen that the shock pressures measured in the experiments and predicted by Chinook are generally significantly lower than the theoretical shock pressures. This is as expected since the gauges used in the experiments were developed for measuring the bubble collapse events and not the shock front. Figure 14(b) shows that the magnitude of the first bubble collapse pressure decreases for standoffs between 0.2R and 0.6R as the standoff increases. This is followed by an increase in bubble collapse pressure up to a standoff of 1.0R at which point the pressures decrease with increasing standoff. Although the peak pressures are poorly predicted by Chinook, the trend in the pressure magnitude observed in the experiments is captured in the simulations. This is more pronounced in the three dimensional models and the coarse two-dimensional model, which were found to predict the bubble dynamics better than the refined two-dimensional simulations. For the second bubble collapse, Figure 17(c), the

experimental results show that the bubble collapse pressure increases with standoff up to a standoff of 1.0R at which point the peak pressures decrease with standoff. For most gauge locations the experimentally measured peak pressure is very close for standoffs between 1.0R and 1.25R, and usually depends on the amount of experimental scatter at the 1.0R standoff. The peak occurs in this range due to the proximity of the gas bubble to the target plate at these standoffs. A similar trend is observed in the Chinook simulation results; however the magnitude of the pressures is significantly larger. The main reason for the larger simulation values is that there is no energy loss in the system, due to the solver's requirement for conservation of energy.

The peak pressures plots for the remaining gauge locations are shown in Appendix B.

5.2.2 Impulse Loading

The impulse time history for the 1.1 g detonator charge at a standoff of 1.0R is shown in Figure 18 for the 5 mm and 50 mm gauge locations.

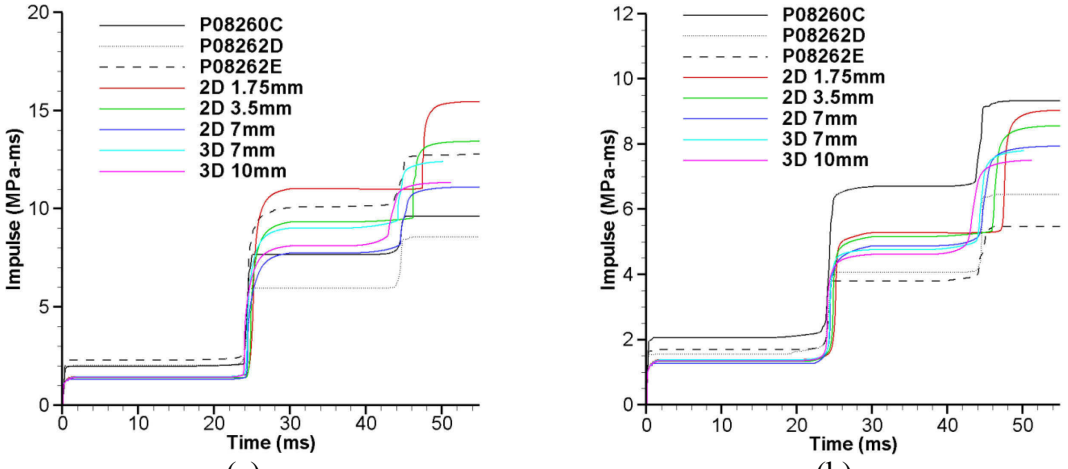

Figure 18: Impulse time history for the 1.1 g detonator at a standoff of 1.0R for the gauge locations of (a) 5 mm, (b) 50 mm

From these figures it can be seen that the range of experimental impulse jumps is relatively large. The difference between the highest and lowest for the first bubble collapse is 3.86 MPa-ms and 2.54 MPa-ms for the 5 mm and 50 mm gauge locations respectively. A similar range of experimental results is observed for the second bubble collapse. A slightly smaller range of impulse jumps was observed among the numerical simulation models. These were found to decrease as the gauge location was moved further from the center of the target.

Figure 19 through Figure 21 compare the shock and bubble collapse impulse jumps for all standoffs at various gauge locations. The impulse plots for the remaining gauge locations are shown in Appendix C.

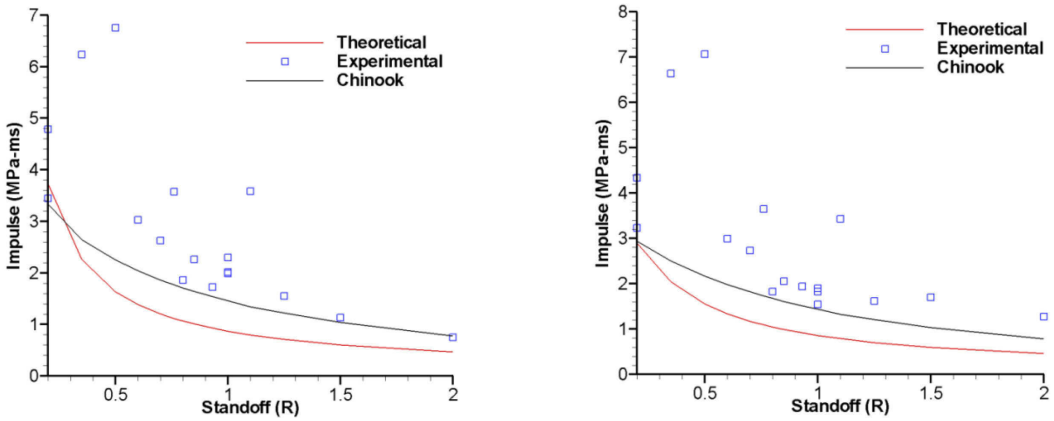

Figure 19: Comparison of the shock impulse as a function of the standoff for the 1.1 g detonator at gauge locations of (a) 5 mm, (b) 25 mm

For all gauge locations Chinook under predicted the shock impulse compared to the experimental values and over predicted the theoretical shock impulses. The shock impulse predictions from the Chinook simulations were found to be in better agreement with the experiments for standoffs greater than 0.8R, with the exception of 1.1R which shows a considerable difference at all gauge locations. The shock impulse was found to be extremely high for the experiments conducted with standoffs of 0.35R and 0.5R.

The Chinook simulations provide the same trends for the first bubble collapse as seen in the experimental results. For the experiments an increase in the impulse was observed from the 0.2R standoff up to 0.8R or 0.85R. The impulse then decreases for standoffs larger than 0.85R. The Chinook simulations show a slight decrease in the impulse from 0.2R to 0.35R but increases up to a standoff of 0.85R to 1.0R, depending on the gauge location. The Chinook impulse decreases with standoffs larger than 1.0R. For the 50 mm gauge location the trend of the experimental data was not predicted by Chinook, which does not show a peak at standoffs between 0.85R and 1.0R but generally decreases as the standoff increased. This results in poor agreement at the 50 mm gauge location.

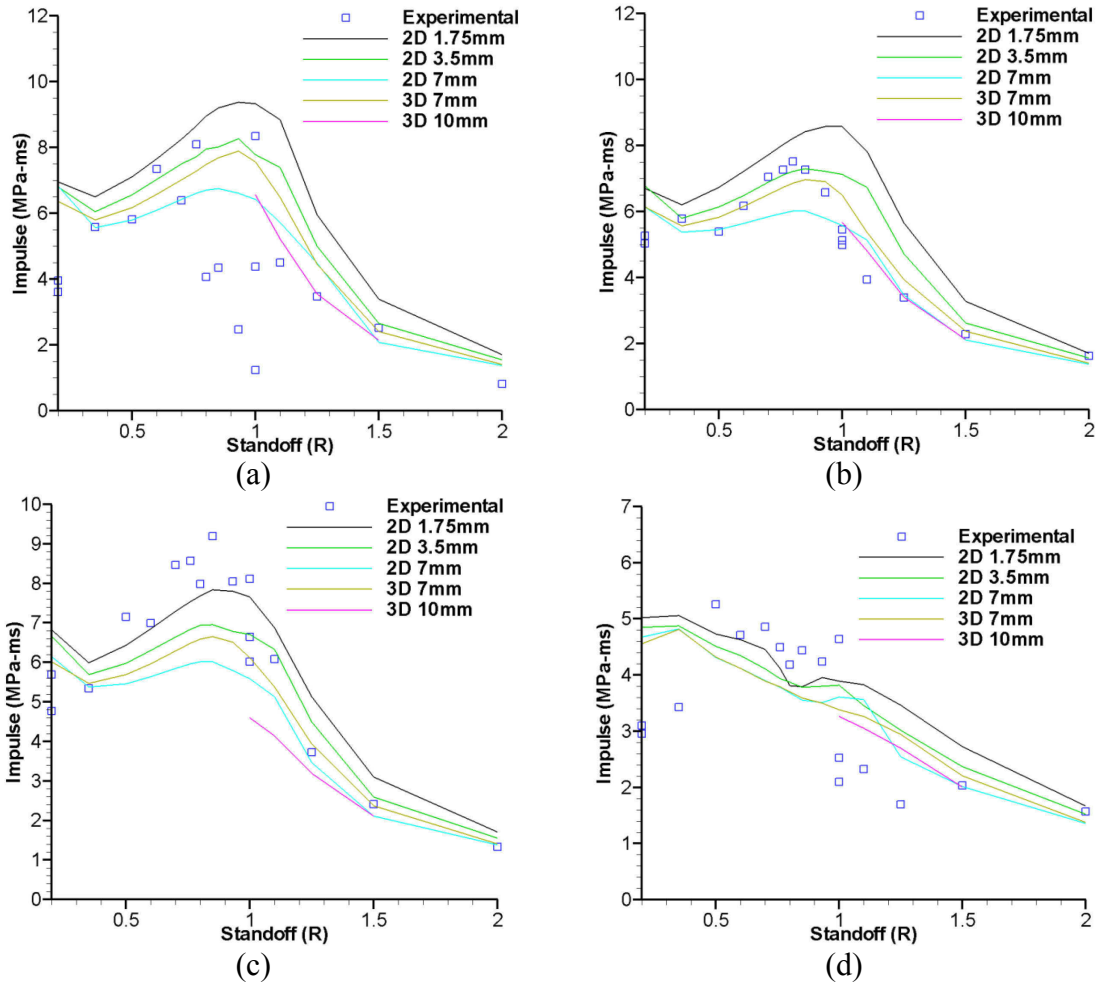

Figure 20: Comparison of the first bubble collapse impulse as a function of the standoff for the 1.1 g detonator at gauge locations of (a) 0 mm, (b) 10 mm, (c) 20 mm, (d) 50 mm

For the 0 mm gauge location agreement between impulse predictions and measurements is generally poor for standoffs between 0.8 and 1.0R. The experimental measurements are uncharacteristically low for these standoffs. For the other standoffs the experimental results are generally enveloped by the different Chinook simulations at the 0 mm gauge location. For the 20 mm gauge location the Chinook impulses under predict the experimental values in the peak region between standoffs of 0.5R and 1.0R, but does give good predictions above and below this range. For the remaining gauge locations the Chinook predictions provide reasonable predictions and generally envelope the experimental measurements as seen for the 10 mm gauge location shown in Figure 20(b).

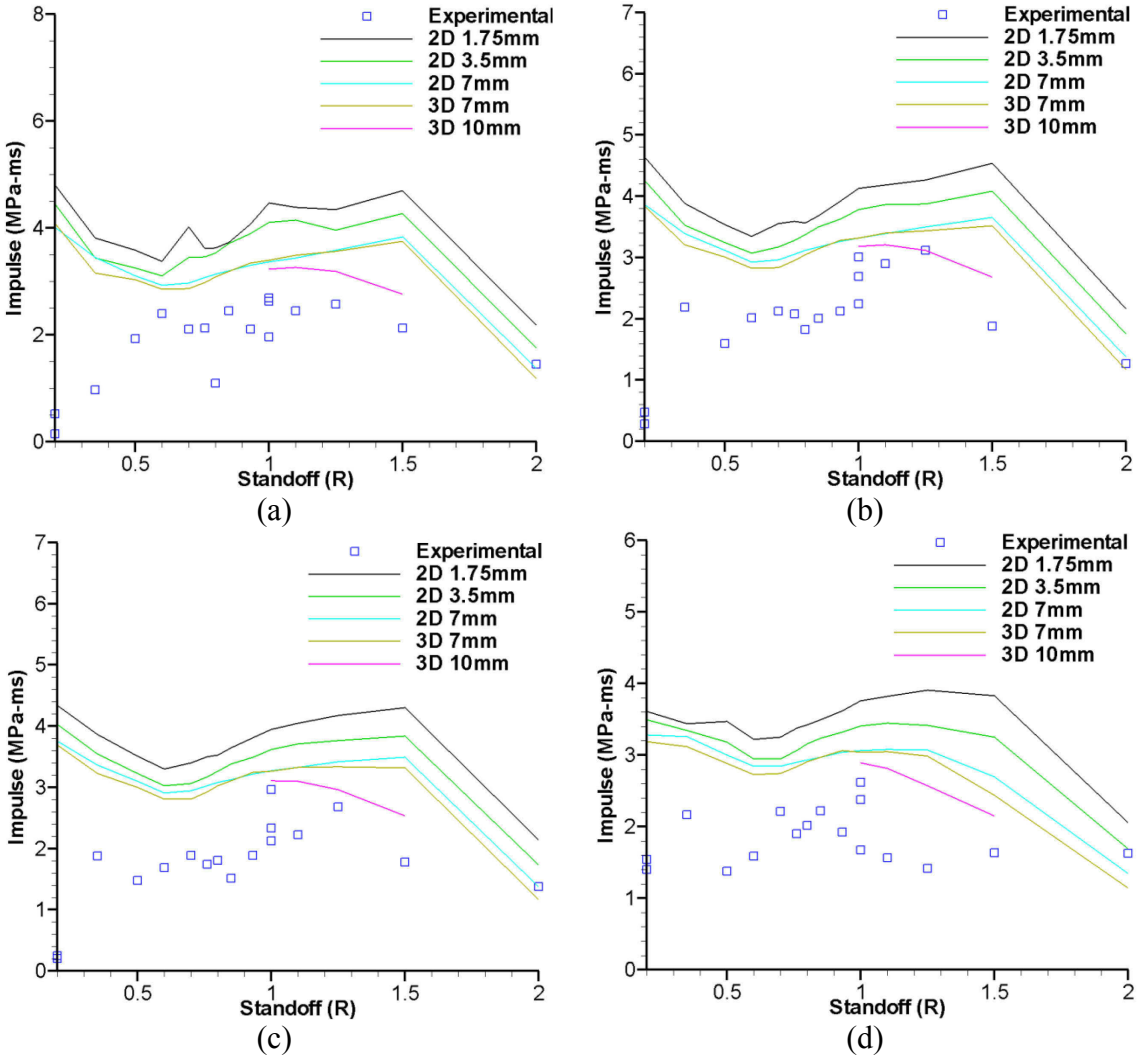

Figure 21: Comparison of the second bubble collapse impulse as a function of standoff for the 1.1 g detonator at gauge locations of (a) 5 mm, (b) 15 mm, (c) 25 mm, (d) 50 mm

The impulse jump for the second bubble collapse is larger in the Chinook simulations than in the experimental measurements. The main source of the higher impulse jump is that Chinook does not apply an energy loss to the gas bubble during the first collapse and migration.

From the experimental results it is difficult to determine if there is a single standoff that generates the largest second bubble collapse loading, however the peak is generally between 1.0R and 1.25R. For the Chinook simulations the peak impulse occurs at a standoff of 1.5R. From the experimental high speed videos it was observed that the bubble is in contact with the target for the second collapse for standoffs up to 1.25R, with the bubble being just above the target for a standoff of 1.5R. In the Chinook simulations, the gas bubble is in contact with the target at the time of the second collapse for an original standoff of 1.5R because of the migration during the first collapse.

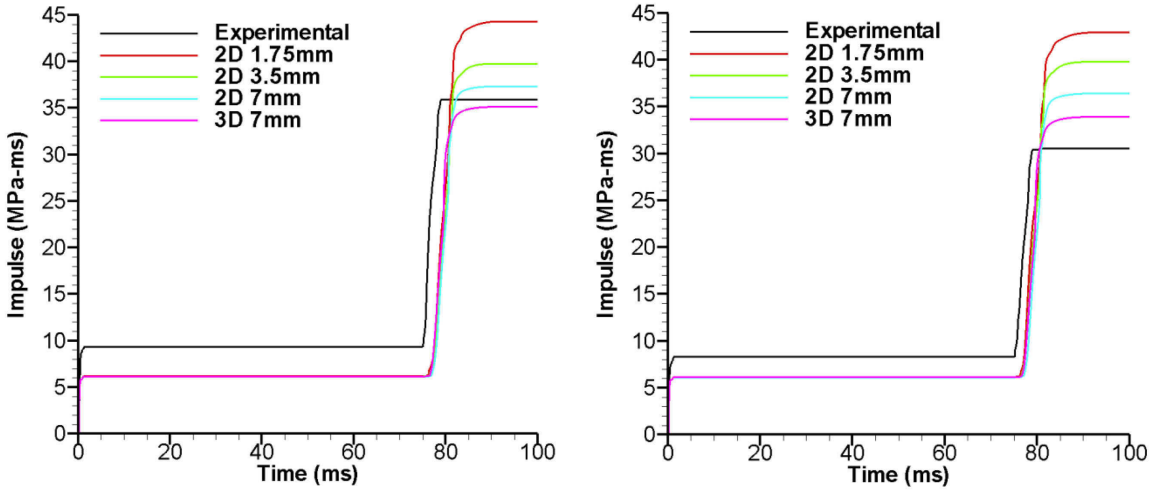

Figure 22: Impulse time history for the 40 g C4 charge at a standoff of 0.6R for the (a) 5 mm gauge, (b) 25 mm gauge

The impulse time history for the 40 g C4 charge is shown in Figure 22. Similar to the detonator charges the increase in impulse is larger in the Chinook simulations than that observed in the experiments. The three-dimensional models predict impulse jumps closest to the experimental measurements, with the difference between the predictions and experiments increasing at locations further from the plate center. Figure 23 compares the first bubble collapse impulse for the two different charges at a standoff of 0.6R.

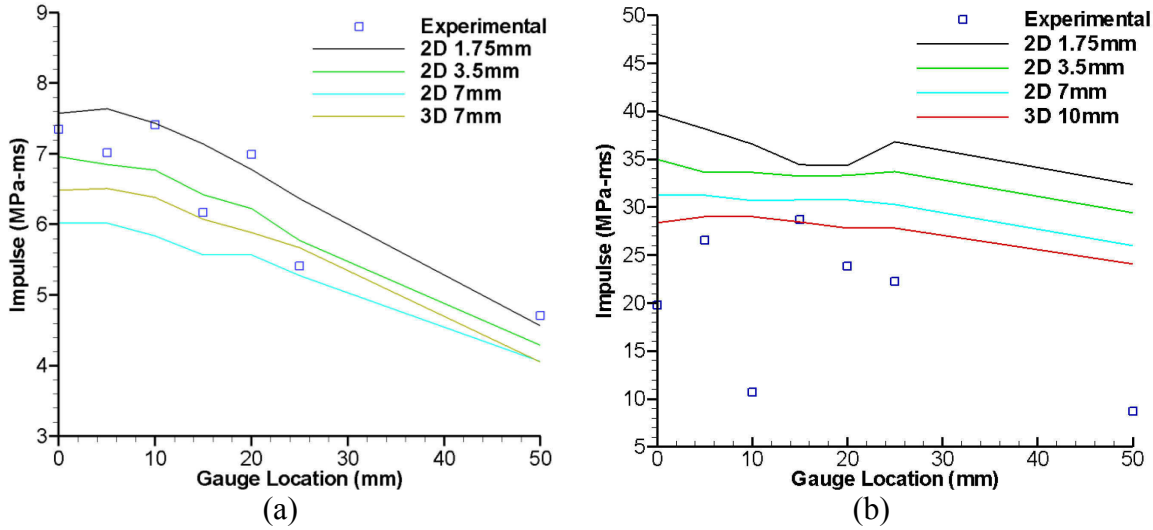

Figure 23: Comparison of first bubble collapse increase in impulse as a function of gauge location for a standoff of 0.6R (a) 1.1 g Detonator (b) 40 g C4 charge

In Figure 23 the 40 g C4 charge shows larger discrepancies from the experiments than the 1.1 g detonator at the same standoff. The variation in the measurements between the

different gauge locations was also significantly larger for the 40 g C4 charge experiments.

6 Conclusion

An extensive numerical modelling study was conducted using the computational fluids dynamic code Chinook to determine its capability to accurately predict the loading on rigid plates subjected to a series of underwater explosions with standoffs ranging from 0.2R up to 2.0R. Chinook predictions of the peak pressure, impulse jump, and time to peak pressure for the first two bubble collapse events were compared to experimental results. The inconsistencies in the experimental results show that it is not easy to get good consistent measurements from underwater explosion experiments.

Chinook was shown to produce the correct time scale for the bubble collapse events. The difference in the first bubble collapse period between the Chinook simulations and experimental measurements was generally less than 2 percent for the three-dimensional models and within 4 percent for the two-dimensional models. For the second bubble collapse the period varied up to 10 percent for the three dimensional models and 15 percent for the two dimensional models. The difference in the bubble period between Chinook and the experimental measurements decreased from the closest standoff up to a standoff of 0.5R, and then was fairly constant from 0.5R up to 2.0R. The gauge location did not seem to influence the difference in bubble periods.

The bubble radius estimated by Chinook compared well with the bubble radius computed with the similitude equations. The gas bubble radii from Chinook and the similitude equations converge as the standoff was increased. The maximum bubble radius for the Chinook simulations was within 7 percent of the similitude fits for all standoffs. For the free-field case the gas bubble radius calculated from Chinook results show good agreement with the free-field similitude value. For the standoffs considered in this study the maximum gas bubble radius slowly approaches the free field similitude value. This shows that the presence of the target affects the bubble formation up to a standoff of 2.0R.

The shock pressures predicted with Chinook were significantly less than those measured at the free field gauges in the experiments. Chinook over-predicted the pressures due to the bubble collapse events compared to the experimentally measured pressures at the embedded gauges.

Compared to the experimental impulses the numerical predictions for the three-dimensional models were generally within 20 percent, with a few values exceeding this mark and more than half being within 10 percent. For the two-dimensional models the first bubble impulse was generally within 20 percent for the coarse two-dimensional mesh, with the refined meshes generally producing larger differences when compared to experiments. The second bubble collapse impulses predicted by Chinook were 2 to 3 times larger than the experimental values. This is expected as Chinook does not predict the energy loss in the gas bubble after the collapse.

Qualitatively Chinook was found to accurately reproduce the general trends in the experimental measurements. Quantitative gaps still remain in the load levels predicted. It was observed that the bubble collapse impulse loading reaches a maximum when the bubble is just contacting the target during collapse. This was observed in both the numerical simulations and experiments. This shows that the bubble migration in Chinook is slightly higher than the experiments, as the bubble collapse impulse peak occurs at a slightly larger standoff than observed in the experiments.

A major issue with Chinook is the lack of a material interface tracker which would allow for the distinction between the gas bubble and the surrounding water. Currently when bubble collapse is simulated, the collapsing bubble is comprised of a material that has a density between water and gas. The inclusion of a material tracker could allow the separation between gas and water to be maintained throughout the collapse and subsequent reformation of the bubble. In this study it was shown that generally the bubble collapse pressures were over-predicted by Chinook compared to experiments. Maintaining the correct bubble density should reduce the pressure loading upon collapse, and thus result in better overall agreement with experiments and better convergence of the two-dimensional models to the experimental results. This is currently being addressed within the Chinook software.

During a presentation of this material at the 81st SAVIAC Symposium, it was brought to the authors' attention that the divergence of the refined models can be influenced significantly by the cut off pressure used to model cavitation. This affects the bubble behaviour because at the bubble's maximum bubble radii, the bubble pressure is very close to the cut off pressure. Currently, the cut-off pressure for controlling cavitation is an internal parameter in Chinook, and cannot be changed by the user. This will be brought to the attention of Martec Ltd.

References

[1] Livermore Software Technology Corporation, 'LS-DYNA Users Manual Version 971', Livermore, CA, USA, 2008.

[2] Martec Ltd., Chinook Manual SM-01-01 Rev 4', Halifax, N.S., Canada, January 2008.

[3] Excel spreadsheet provided through informal communication with Julian Lee at DRDC Suffield

[4] Van Aanhold, J.E. (2010), Simplified models for close-proximity UNDEX, TNO-034-DTM-2009-04888, TNO report, CONFIDENTIAL.

[5] SAS IP Inc., 'ANSYS release 11.0 documentation', Canonsburg, PA, USA, 2008.

[6] Timothy E. Dunbar, 'Modelling of Close-Proximity Underwater Explosion Loads and Structural Response', TR-09-14, Martec Limited, 2009.

[7] Timothy E. Dunbar (2009), 'Modelling of Close-Proximity Underwater Explosion Loads and Structural Response – Phase 2', DRDC Atlantic Contractor Report CR 2009-180.

[8] Mark Riley and Malcolm J. Smith (2010), 'Modeling of Shock and Bubble collapse Loading on a Rigid target Due to Underwater Explosions: Comparison to experiments Conducted at FOI Grindsjön', DRDC Atlantic Technical Memorandum TM 2009-270.

[9] Klaseboer, E., Hung, K.C., Wang, C., Wang, C.W., Khoo, B.C., Boyce, P., Debono, S., Charlier, H., 'Experimental and Numerical investigation of the dynamics of an underwater explosion bubble near a resilient/rigid structure', Journal of Fluid Mechanics, Vol. 537, pp. 387-413, 2005.

This page intentionally left blank.

Annex A Bubble Period Results

The tables in this Annex compare the gas bubble periods at the different gauge locations for the similitude equations, experiments, and simulations conducted in this study. The second theoretical gas bubble period is based on the similitude period for the second bubble cycle with the energy loss function applied.

Table 7: Theoretical, experimental, and numerical first bubble periods for the 0mm gauge location

Charge Geometry		Theoretical (ms)	Experimental (ms)	Chinook (ms)				
				2D			3D	
Charge	Standoff (mm)			1.75 mm	3.5 mm	7 mm	7mm	10 mm
RP-83	28	22.82	25.01	26.33	26.12	25.85	25.67	
	49	22.85	25.10	26.19	25.95	25.66	25.56	
	70	22.87	25.15	26.14	25.88	25.46	25.46	
	84	22.89	25.11	26.06	25.78	25.37	25.36	
	98	22.9	24.35	25.95	25.63	25.21	25.18	N/A
	106	22.91	24.90	25.79	25.50	25.10	25.07	
	112	22.92	24.59	25.84	25.40	25.00	24.95	
	119	22.93	24.51	25.54	25.27	24.85	24.83	
	130	22.94	24.63	25.31	25.05	24.68	24.60	
	140	22.95	24.61	25.17	24.82	24.42	24.35	24.01
	154	22.97	24.15	24.84	24.54	24.22	24.16	23.84
	175	22.99	23.70	24.43	24.15	23.88	23.77	23.49
	210	23.04	23.33	23.94	23.72	23.48	23.38	23.17
	280	23.12	23.06	23.50	23.32	23.09	23.02	N/A
40 g C4	300	75.53	75.87	81.45	81.33	80.61	N/A	79.62

Table 8: Theoretical, experimental, and numerical second bubble periods for the 0mm gauge location

Charge Geometry		Theoretical (ms)	Experimental (ms)	Chinook (ms)				
				2D			3D	
Charge	Standoff (mm)			1.75 mm	3.5 mm	7 mm	7mm	10 mm
RP-83	28	19.10	18.16	22.03	21.59	21.14	20.68	
	49	19.12	17.05	21.10	20.69	20.96	20.42	
	70	19.14	17.39	20.57	20.25	20.04	19.58	
	84	19.15	17.91	20.52	19.57	19.95	19.40	
	98	19.17	18.83	20.69	20.03	19.16	18.81	N/A
	106	19.18	17.69	20.94	20.32	19.40	19.12	
	112	19.18	19.62	21.00	20.58	19.59	19.32	
	119	19.19	20.15	21.50	20.83	19.76	19.54	
	130	19.20	19.89	21.96	21.11	20.06	19.83	
	140	19.21	20.19	22.26	21.38	20.17	19.88	19.02
	154	19.22	20.57	22.57	21.53	20.29	19.93	19.06
	175	19.25	20.30	22.75	21.41	20.38	19.81	19.08
	210	19.28	18.79	22.22	20.97	19.68	18.73	17.91
	280	19.35	16.63	19.53	18.81	18.18	17.44	N/A

Table 9: Theoretical, experimental, and numerical first bubble periods for the 5mm gauge location

Charge Geometry		Theoretical (ms)	Experimental (ms)	Chinook (ms)				
				2D			3D	
Charge	Standoff (mm)			1.75 mm	3.5 mm	7 mm	7mm	10 mm
RP-83	28	22.82	25.06	26.33	26.12	25.85	25.67	
	49	22.85	25.12	26.19	25.95	25.66	25.56	
	70	22.87	25.15	26.14	25.89	25.46	25.46	
	84	22.89	25.13	26.06	25.78	25.37	25.36	
	98	22.9	25.03	25.95	25.63	25.21	25.18	N/A
	106	22.91	24.90	25.79	25.50	25.10	25.07	
	112	22.92	24.72	25.84	25.41	25.00	24.95	
	119	22.93	24.65	25.54	25.27	24.85	24.83	
	130	22.94	24.49	25.31	25.05	24.68	24.60	
	140	22.95	24.46	25.17	24.82	24.42	24.35	24.01
	154	22.97	24.08	24.84	24.54	24.22	24.16	23.84
	175	22.99	23.69	24.43	24.15	23.88	23.77	23.49
	210	23.04	23.35	23.94	23.72	23.48	23.38	23.17
	280	23.12	22.97	23.50	23.32	23.09	23.02	N/A
40 g C4	300	75.53	75.79	81.70	81.33	80.61	N/A	79.62

Table 10: Theoretical, experimental, and numerical second bubble periods for the 5mm gauge location

Charge Geometry		Theoretical (ms)	Experimental (ms)	Chinook (ms)				
				2D			3D	
Charge	Standoff (mm)			1.75 mm	3.5 mm	7 mm	7mm	10 mm
RP-83	28	19.10	17.66	22.03	21.60	21.14	20.68	
	49	19.12	17.14	21.41	20.69	20.96	20.42	
	70	19.14	17.57	20.57	20.24	20.04	19.58	
	84	19.15	17.86	20.21	19.57	19.95	19.40	
	98	19.17	18.60	20.69	20.03	19.16	18.82	N/A
	106	19.18	18.71	20.94	20.32	19.40	19.12	
	112	19.18	19.18	21.00	20.57	19.59	19.32	
	119	19.19	19.83	21.50	20.83	19.76	19.54	
	130	19.20	18.53	21.96	21.11	20.06	19.83	
	140	19.21	20.31	22.26	21.39	20.17	19.88	19.02
	154	19.22	20.65	22.57	21.53	20.29	19.93	19.06
	175	19.25	20.35	22.76	21.42	20.38	19.81	19.08
	210	19.28	18.77	22.22	20.98	19.68	18.73	17.91
	280	19.35	16.33	19.53	18.81	18.18	17.44	N/A

Table 11: Theoretical, experimental, and numerical first bubble periods for the 10mm gauge location

Charge Geometry		Theoretical (ms)	Experimental (ms)	Chinook (ms)				
				2D			3D	
Charge	Standoff (mm)			1.75 mm	3.5 mm	7 mm	7mm	10 mm
RP-83	28	22.82	24.99	26.33	26.11	25.85	25.67	
	49	22.85	25.12	26.19	25.96	25.66	25.56	
	70	22.87	25.20	26.14	25.89	25.46	25.45	
	84	22.89	25.12	26.07	25.78	25.37	25.36	
	98	22.9	25.03	25.95	25.64	25.21	25.19	N/A
	106	22.91	24.87	25.79	25.50	25.10	25.07	
	112	22.92	24.66	25.84	25.41	25.00	24.95	
	119	22.93	24.60	25.54	25.27	24.85	24.84	
	130	22.94	24.50	25.31	25.05	24.68	24.60	
	140	22.95	24.44	25.17	24.82	24.42	24.35	24.01
	154	22.97	24.09	24.84	24.54	24.22	24.16	23.84
	175	22.99	23.70	24.43	24.15	23.88	23.77	23.49
	210	23.04	23.33	23.94	23.72	23.48	23.38	23.17
	280	23.12	22.97	23.50	23.32	23.09	23.02	N/A
40 g C4	300	75.53	75.82	81.70	81.34	80.61	N/A	79.62

Table 12: Theoretical, experimental, and numerical second bubble periods for the 10mm gauge location

Charge Geometry		Theoretical (ms)	Experimental (ms)	Chinook (ms)				
				2D			3D	
Charge	Standoff (mm)			1.75 mm	3.5 mm	7 mm	7mm	10 mm
RP-83	28	19.10	17.88	22.03	21.62	21.14	20.69	N/A
	49	19.12	17.19	21.41	20.68	20.96	20.42	
	70	19.14	17.50	20.57	20.24	20.04	19.59	
	84	19.15	17.87	20.20	19.57	19.95	19.41	
	98	19.17	18.51	20.69	20.02	19.15	18.81	
	106	19.18	17.52	20.93	20.32	19.40	19.12	
	112	19.18	19.33	21.01	20.57	19.60	19.33	
	119	19.19	19.90	21.50	20.82	19.76	19.53	
	130	19.20	19.70	21.95	21.10	20.07	19.84	
	140	19.21	20.31	22.25	21.39	20.17	19.88	19.02
	154	19.22	20.20	22.57	21.53	20.29	19.93	19.07
	175	19.25	20.29	22.76	21.42	20.39	19.81	19.08
	210	19.28	19.06	22.23	20.98	19.68	18.73	17.91
	280	19.35	16.29	19.53	18.81	18.18	17.44	N/A

Table 13: Theoretical, experimental, and numerical first bubble periods for the 15mm gauge location

Charge Geometry		Theoretical (ms)	Experimental (ms)	Chinook (ms)				
				2D			3D	
Charge	Standoff (mm)			1.75 mm	3.5 mm	7 mm	7mm	10 mm
RP-83	28	22.82	24.87	26.32	26.11	25.86	25.66	N/A
	49	22.85	25.07	26.20	25.96	25.66	25.57	
	70	22.87	25.15	26.14	25.89	25.46	25.46	
	84	22.89	25.07	26.07	25.79	25.38	25.37	
	98	22.9	25.03	25.94	25.64	25.21	25.19	
	106	22.91	24.90	25.79	25.50	25.10	25.08	
	112	22.92	24.73	25.68	25.41	25.01	24.96	
	119	22.93	24.69	25.54	25.27	24.86	24.84	
	130	22.94	24.50	25.31	25.04	24.68	24.60	
	140	22.95	24.40	25.16	24.82	24.42	24.35	24.01
	154	22.97	24.06	24.84	24.54	24.22	24.16	23.84
	175	22.99	23.69	24.43	24.15	23.88	23.77	23.49
	210	23.04	23.33	23.94	23.72	23.48	23.38	23.17
	280	23.12	22.90	23.50	23.32	23.09	23.02	N/A
40 g C4	300	75.53	78.18	81.70	80.76	80.61	N/A	79.62

Table 14: Theoretical, experimental, and numerical second bubble periods for the 15mm gauge location

Charge Geometry		Theoretical (ms)	Experimental (ms)	Chinook (ms)				
				2D			3D	
Charge	Standoff (mm)			1.75 mm	3.5 mm	7 mm	7mm	10 mm
RP-83	28	19.10	18.19	22.05	21.63	21.14	20.72	N/A
	49	19.12	17.20	21.40	20.69	20.97	20.42	
	70	19.14	17.56	20.57	20.24	20.04	19.58	
	84	19.15	17.86	20.18	19.57	19.95	19.40	
	98	19.17	18.55	20.71	20.02	19.16	18.82	
	106	19.18	18.84	20.93	20.31	19.41	19.12	
	112	19.18	19.24	21.15	20.55	19.59	19.32	
	119	19.19	19.63	21.48	20.81	19.76	19.53	
	130	19.20	18.37	21.94	21.10	20.07	19.84	
	140	19.21	20.33	22.25	21.39	20.18	19.89	19.03
	154	19.22	20.19	22.57	21.53	20.30	19.94	19.07
	175	19.25	20.31	22.76	21.42	20.40	19.83	19.08
	210	19.28	19.08	22.23	20.98	19.67	18.72	17.91
	280	19.35	16.31	19.53	18.81	18.18	17.44	N/A

Table 15: Theoretical, experimental, and numerical first bubble periods for the 20mm gauge location

Charge Geometry		Theoretical (ms)	Experimental (ms)	Chinook (ms)				
				2D			3D	
Charge	Standoff (mm)			1.75 mm	3.5 mm	7 mm	7mm	10 mm
RP-83	28	22.82	24.96	26.32	26.11	25.86	25.68	N/A
	49	22.85	25.11	26.20	25.96	25.66	25.57	
	70	22.87	25.14	26.15	25.89	25.46	25.47	
	84	22.89	25.09	26.07	25.79	25.38	25.37	
	98	22.9	25.03	25.94	25.64	25.21	25.19	
	106	22.91	24.87	25.79	25.51	25.10	25.08	
	112	22.92	24.69	25.68	25.41	25.01	24.96	
	119	22.93	24.65	25.54	25.28	24.86	24.84	
	130	22.94	24.49	25.32	25.04	24.68	24.59	
	140	22.95	24.43	25.16	24.82	24.42	24.35	24.01
	154	22.97	24.09	24.84	24.54	24.22	24.16	23.84
	175	22.99	23.69	24.43	24.15	23.88	23.77	23.49
	210	23.04	23.33	23.94	23.72	23.48	23.38	23.17
	280	23.12	23.02	23.50	23.32	23.09	23.02	N/A
40 g C4	300	75.53	78.21	81.70	80.76	80.61	N/A	79.62

Table 16: Theoretical, experimental, and numerical second bubble periods for the 20mm gauge location

Charge Geometry		Theoretical (ms)	Experimental (ms)	Chinook (ms)				
				2D			3D	
Charge	Standoff (mm)			1.75 mm	3.5 mm	7 mm	7mm	10 mm
RP-83	28	19.10	17.99	22.06	21.64	21.14	20.71	N/A
	49	19.12	17.12	21.40	20.70	20.97	20.42	
	70	19.14	17.57	20.57	20.24	20.04	19.57	
	84	19.15	17.94	20.17	19.57	19.95	19.41	
	98	19.17	18.50	20.71	20.03	19.16	18.82	
	106	19.18	18.91	20.92	20.32	19.41	19.12	
	112	19.18	19.31	21.14	20.55	19.59	19.33	
	119	19.19	19.44	21.48	20.79	19.76	19.54	
	130	19.20	19.66	21.92	21.13	20.07	19.85	
	140	19.21	20.30	22.28	21.39	20.18	19.89	19.06
	154	19.22	20.12	22.58	21.53	20.30	19.94	19.10
	175	19.25	20.29	22.77	21.43	20.40	19.83	19.07
	210	19.28	19.34	22.24	20.99	19.67	18.72	17.91
	280	19.35	16.66	19.53	18.81	18.18	17.44	N/A

Table 17: Theoretical, experimental, and numerical first bubble periods for the 25mm gauge location

Charge Geometry		Theoretical (ms)	Experimental (ms)	Chinook (ms)				
				2D			3D	
Charge	Standoff (mm)			1.75 mm	3.5 mm	7 mm	7mm	10 mm
RP-83	28	22.82	24.99	26.32	26.11	25.86	25.69	N/A
	49	22.85	25.09	26.20	25.97	25.67	25.57	
	70	22.87	25.14	26.15	25.90	25.47	25.47	
	84	22.89	25.07	26.08	25.79	25.38	25.37	
	98	22.9	25.04	25.94	25.65	25.22	25.19	
	106	22.91	24.90	25.79	25.47	25.11	25.08	
	112	22.92	24.75	25.68	25.38	25.01	24.96	
	119	22.93	24.73	25.55	25.28	24.86	24.83	
	130	22.94	24.50	25.39	25.04	24.68	24.59	
	140	22.95	24.42	25.16	24.82	24.43	24.35	24.01
	154	22.97	24.09	24.84	24.54	24.22	24.16	23.84
	175	22.99	23.67	24.43	24.16	23.88	23.77	23.49
	210	23.04	23.33	23.94	23.72	23.48	23.38	23.17
	280	23.12	22.92	23.50	23.32	23.09	23.02	N/A
40 g C4	300	75.53	78.17	81.70	80.76	80.61	N/A	79.62

Table 18: Theoretical, experimental, and numerical second bubble periods for the 25mm gauge location

Charge Geometry		Theoretical (ms)	Experimental (ms)	Chinook (ms)				
				2D			3D	
Charge	Standoff (mm)			1.75 mm	3.5 mm	7 mm	7mm	10 mm
RP-83	28	19.10	17.70	22.07	21.66	21.16	20.71	N/A
	49	19.12	16.83	21.39	21.17	20.95	20.42	
	70	19.14	17.56	20.57	20.22	20.03	19.56	
	84	19.15	17.85	20.14	19.58	19.91	19.36	
	98	19.17	18.46	20.72	20.02	19.15	18.83	
	106	19.18	18.83	20.91	20.37	19.41	19.13	
	112	19.18	19.30	21.14	20.61	19.60	19.33	
	119	19.19	19.48	21.46	20.83	19.76	19.55	
	130	19.20	18.39	21.84	21.13	20.08	19.86	
	140	19.21	20.32	22.29	21.40	20.18	19.89	19.06
	154	19.22	20.63	22.58	21.54	20.31	19.95	19.10
	175	19.25	20.35	22.77	21.42	20.41	19.84	19.07
	210	19.28	18.80	22.24	21.00	19.62	18.72	17.91
	280	19.35	16.25	19.54	18.81	18.18	17.44	N/A

Table 19: Theoretical, experimental, and numerical first bubble periods for the 50mm gauge location

Charge Geometry		Theoretical (ms)	Experimental (ms)	Chinook (ms)				
				2D			3D	
Charge	Standoff (mm)			1.75 mm	3.5 mm	7 mm	7mm	10 mm
RP-83	28	22.82	24.94	26.33	26.13	25.88	25.70	N/A
	49	22.85	25.13	26.19	25.95	25.63	25.54	
	70	22.87	25.19	26.17	25.92	25.40	25.42	
	84	22.89	25.13	26.03	25.74	25.32	25.33	
	98	22.9	25.04	25.92	25.60	25.16	25.14	
	106	22.91	24.84	25.78	25.46	25.06	25.04	
	112	22.92	24.72	25.67	25.38	24.98	24.94	
	119	22.93	24.71	25.59	25.26	24.85	24.83	
	130	22.94	24.48	25.38	25.04	24.70	24.61	
	140	22.95	24.26	25.16	24.82	24.44	24.37	24.03
	154	22.97	24.02	24.84	24.55	24.23	24.17	23.85
	175	22.99	23.56	24.44	24.16	23.89	23.78	23.50
	210	23.04	23.33	23.95	23.72	23.49	23.38	23.17
	280	23.12	22.93	23.51	23.32	23.10	23.02	N/A
40 g C4	300	75.53	78.18	80.85	80.75	80.62	N/A	79.59

Table 20: Theoretical, experimental, and numerical second bubble periods for the 50mm gauge location

Charge Geometry		Theoretical (ms)	Experimental (ms)	Chinook (ms)				
				2D			3D	
Charge	Standoff (mm)			1.75 mm	3.5 mm	7 mm	7mm	10 mm
RP-83	28	19.10	17.51	22.10	21.74	21.20	20.78	N/A
	49	19.12	17.00	21.35	20.87	20.89	20.34	
	70	19.14	17.59	20.56	20.18	20.11	19.58	
	84	19.15	17.93	20.59	19.65	19.89	19.34	
	98	19.17	18.40	20.76	20.09	19.26	19.52	
	106	19.18	18.94	20.98	20.39	19.49	19.22	
	112	19.18	19.30	21.22	20.63	19.67	19.39	
	119	19.19	19.42	21.49	20.87	19.82	19.59	
	130	19.20	19.66	21.92	21.15	20.11	19.87	
	140	19.21	20.19	22.31	21.42	20.22	19.91	19.13
	154	19.22	20.03	22.61	21.55	20.38	19.99	19.25
	175	19.25	20.41	22.79	21.47	20.50	19.95	19.03
	210	19.28	18.87	22.27	20.90	19.60	18.79	17.93
	280	19.35	16.32	19.53	18.82	18.17	17.45	N/A

Annex B Peak Pressure Plots

The figures in this Annex compare the peak pressures at the different embedded gauge locations for the experiments and simulations conducted in this study. In some instances extraneous points were removed from the plots to allow for the general trend to be seen in the data.

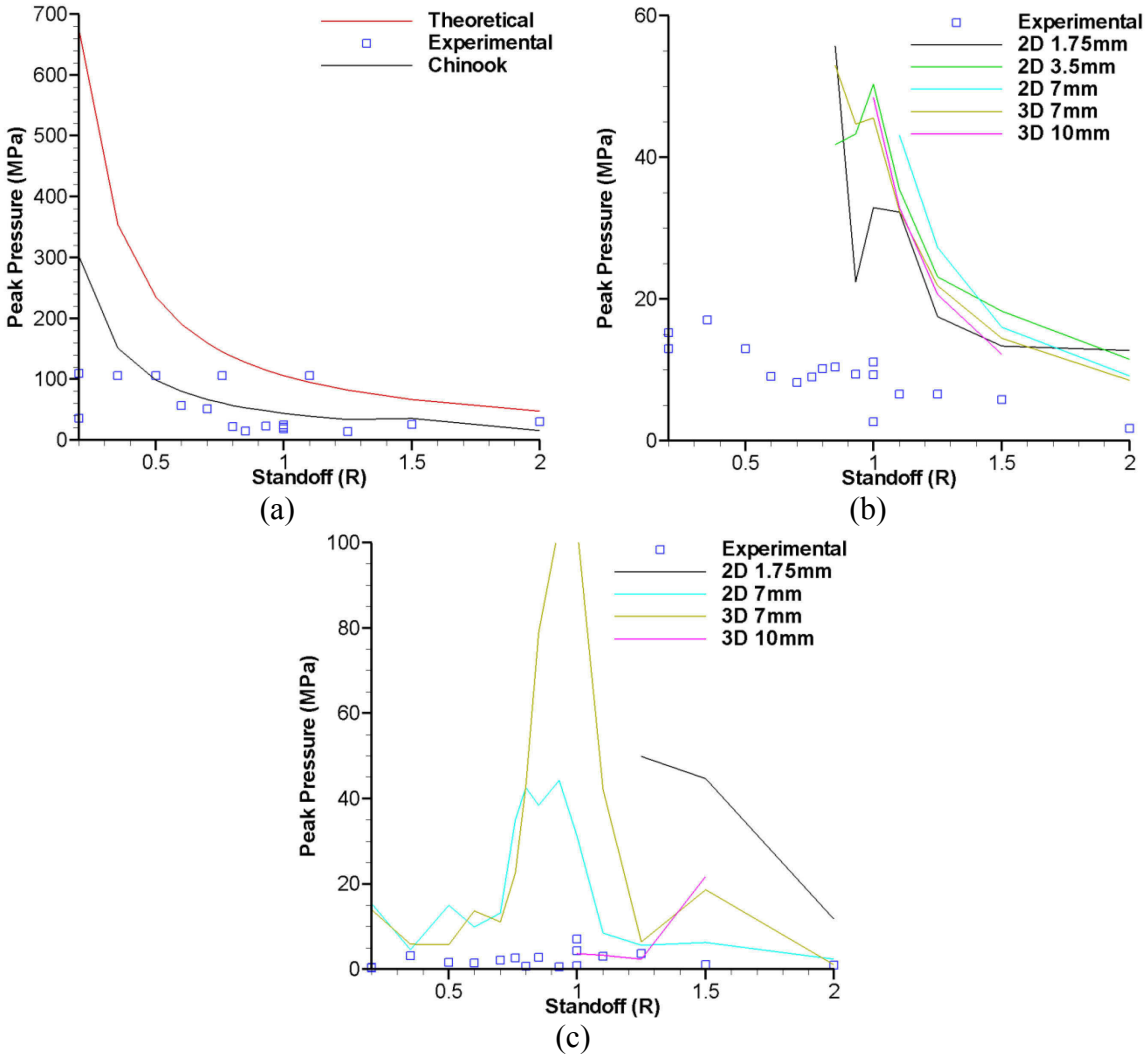

Figure 24: Comparison of the peak pressures as a function of the standoff for the 0 mm gauge location (a) Shock, (b) first bubble collapse, (c) second bubble collapse

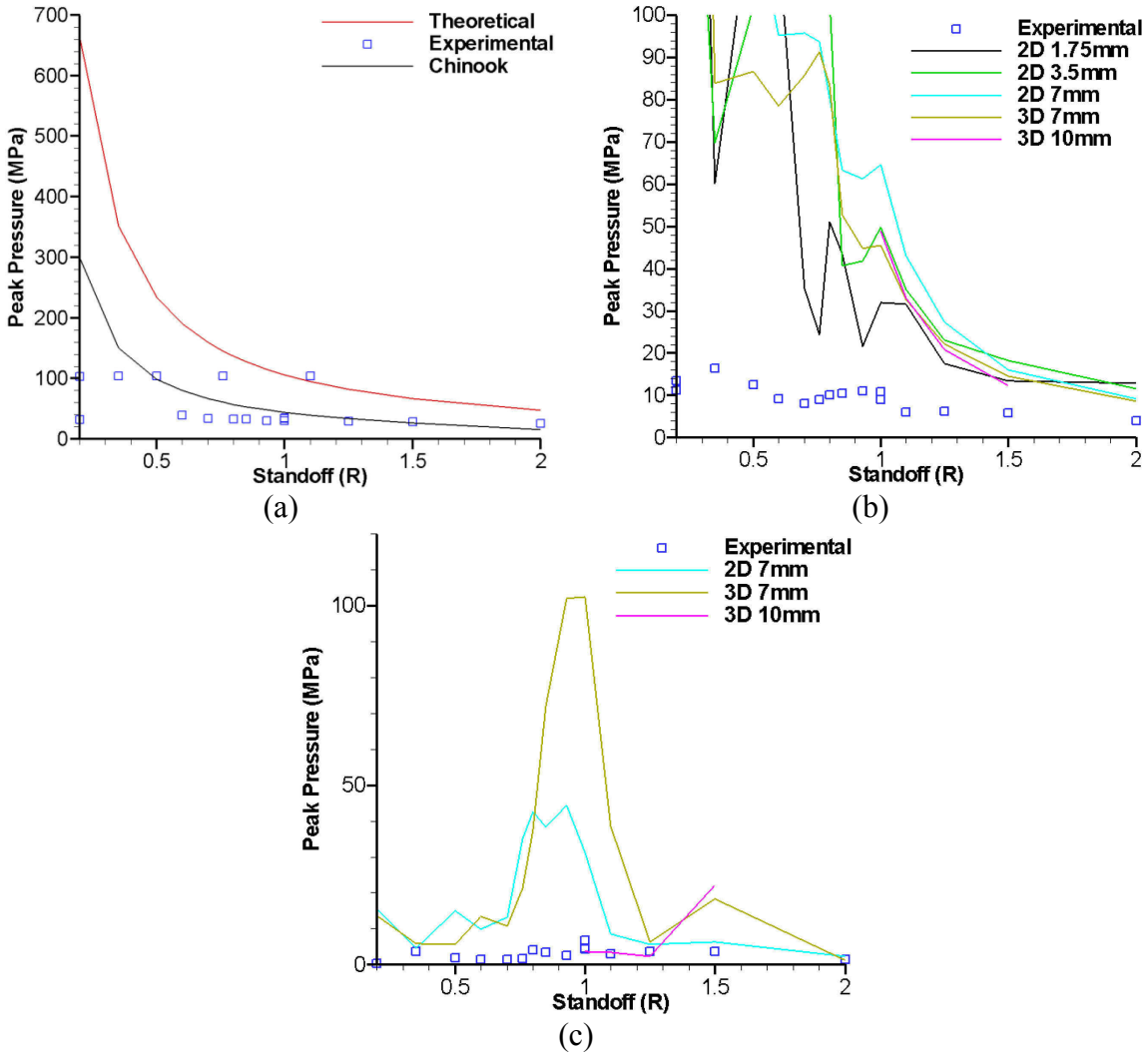

Figure 25: Comparison of the peak pressures as a function of the standoff for the 5 mm gauge location (a) Shock, (b) first bubble collapse, (c) second bubble collapse

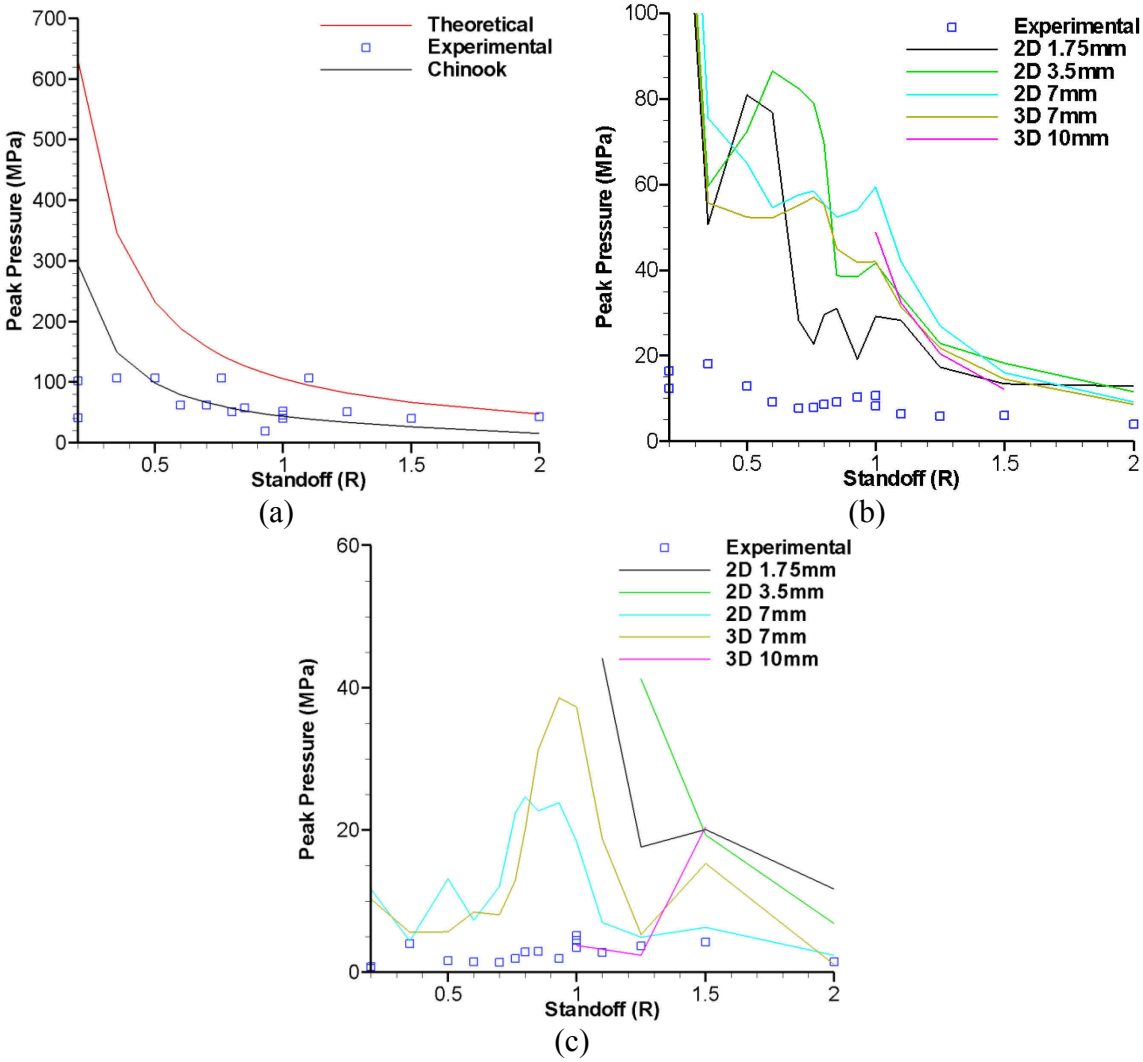

Figure 26: Comparison of the peak pressures as a function of the standoff for the 10 mm gauge location (a) Shock, (b) first bubble collapse, (c) second bubble collapse

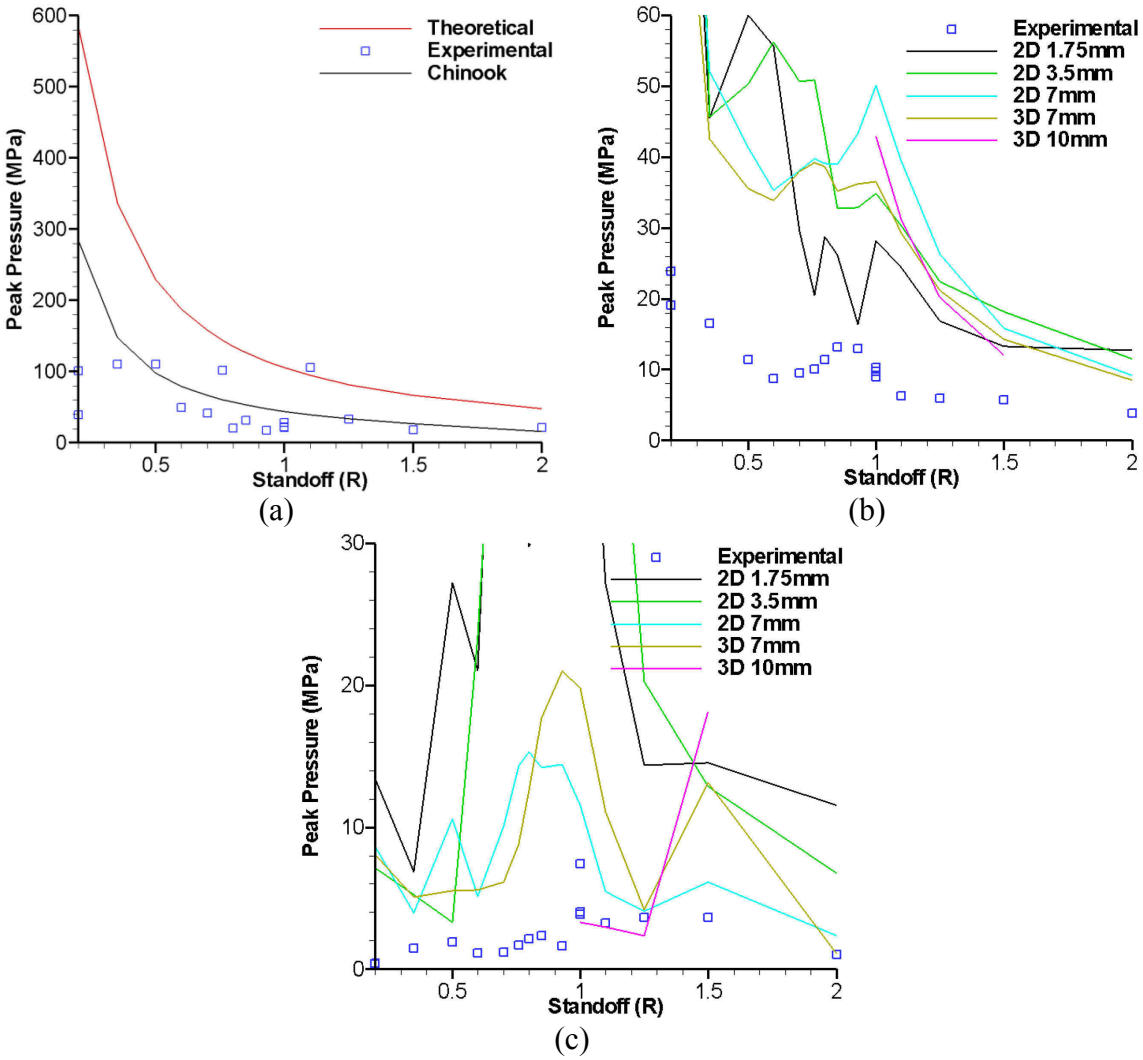

Figure 27: Comparison of the peak pressures as a function of the standoff for the 15 mm gauge location (a) Shock, (b) first bubble collapse, (c) second bubble collapse

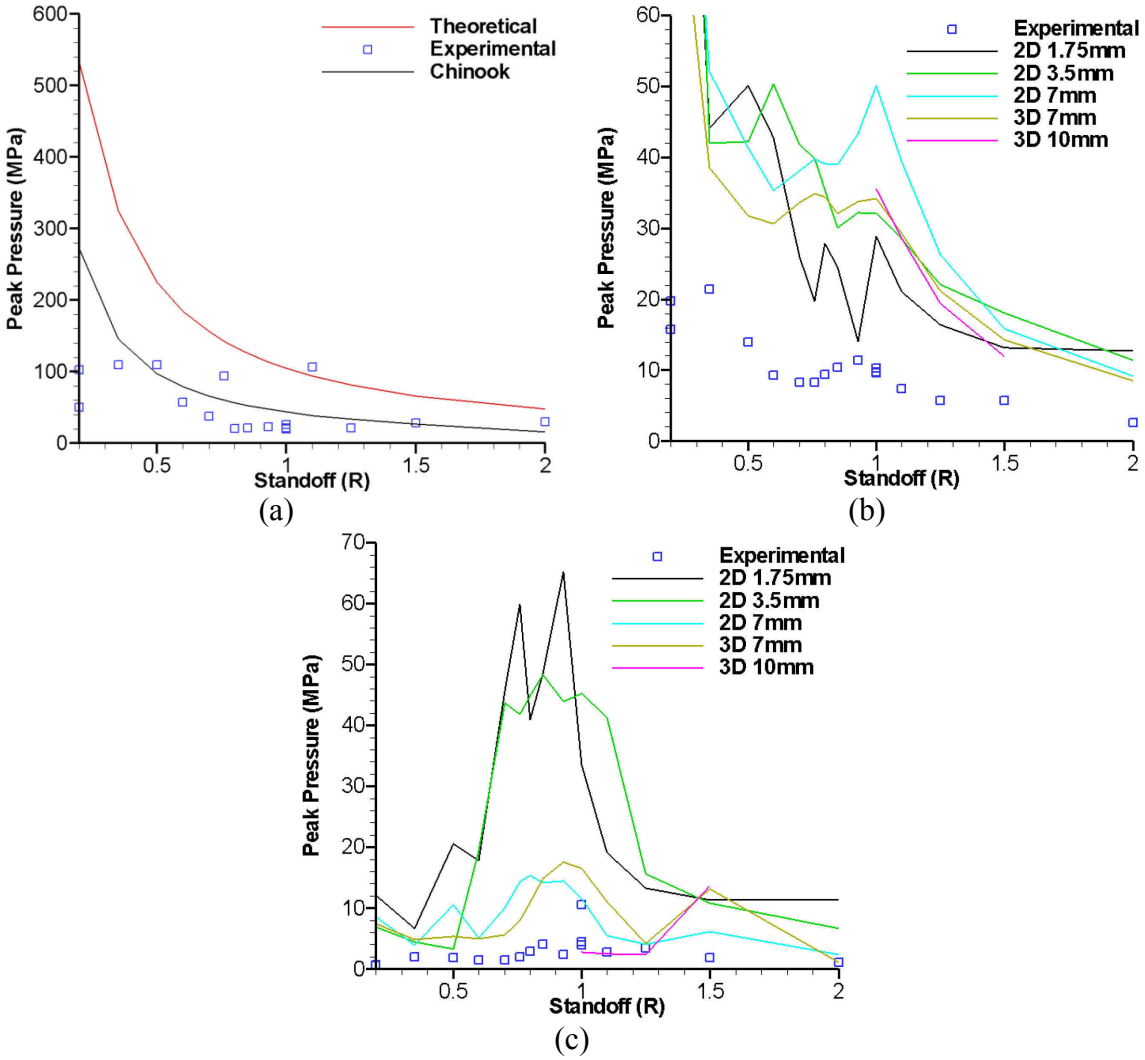

Figure 28: Comparison of the peak pressures as a function of the standoff for the 20 mm gauge location (a) Shock, (b) first bubble collapse, (c) second bubble collapse

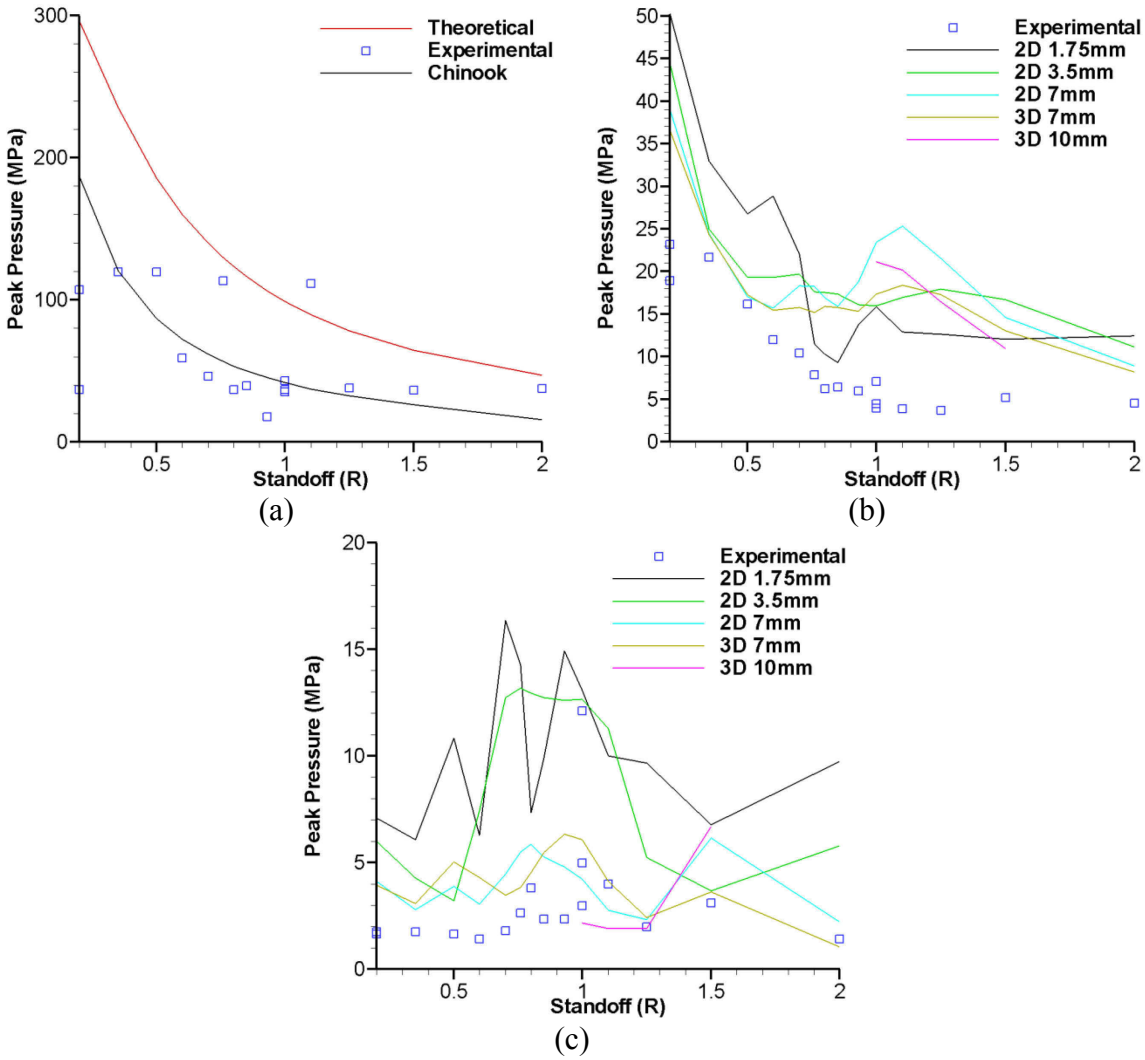

Figure 29: Comparison of the peak pressures as a function of the standoff for the 50 mm gauge location (a) Shock, (b) first bubble collapse, (c) second bubble collapse

Annex C Impulse plots

The figures in this Annex compares the increase in the impulse due to the shock loading and subsequent bubble collapse loadings for the embedded gauges not shown in the main body of the report.

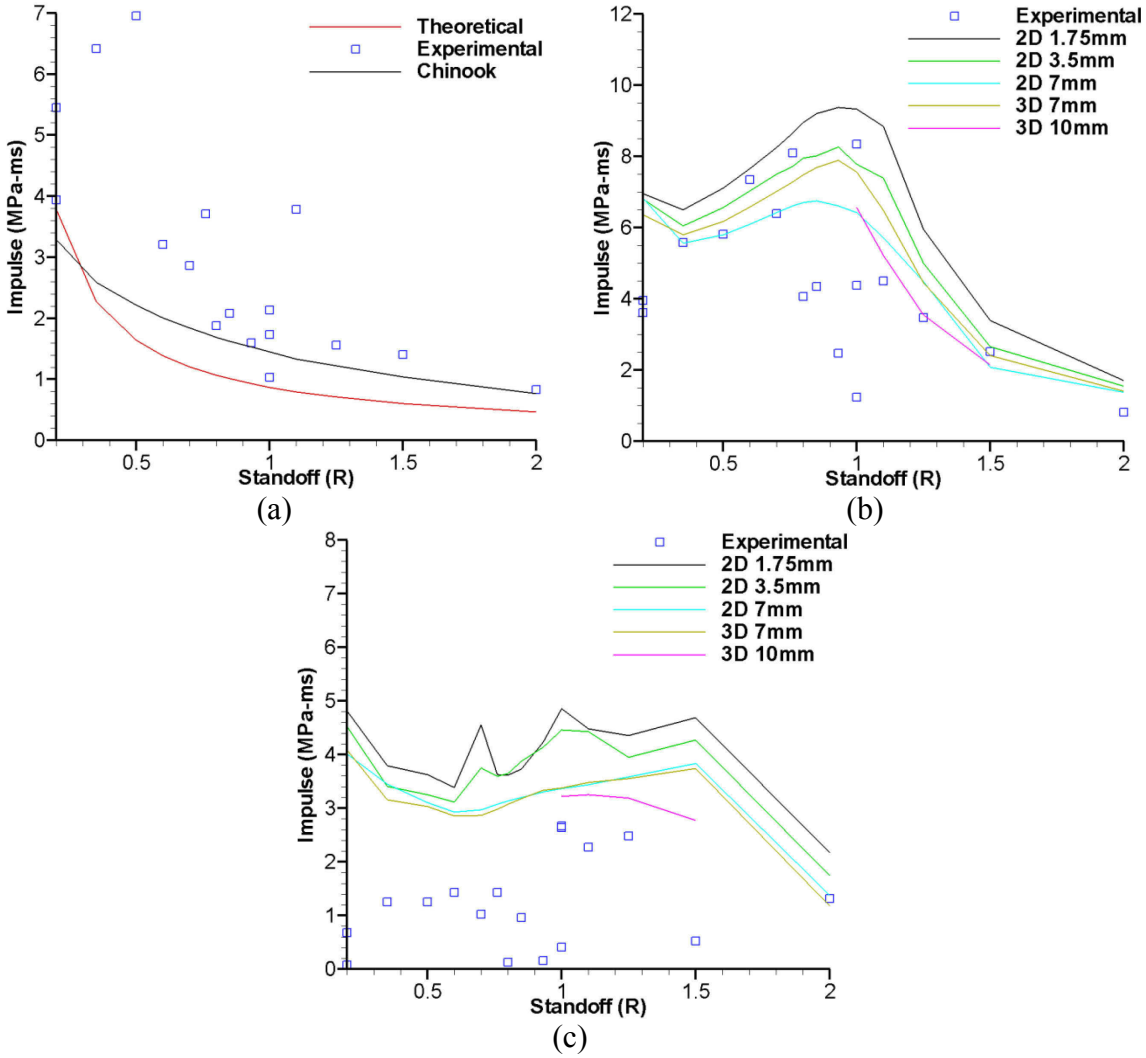

Figure 30: Comparison of the impulse increase as a function of the standoff for the 0 mm gauge location (a) Shock, (b) first bubble collapse, (c) second bubble collapse

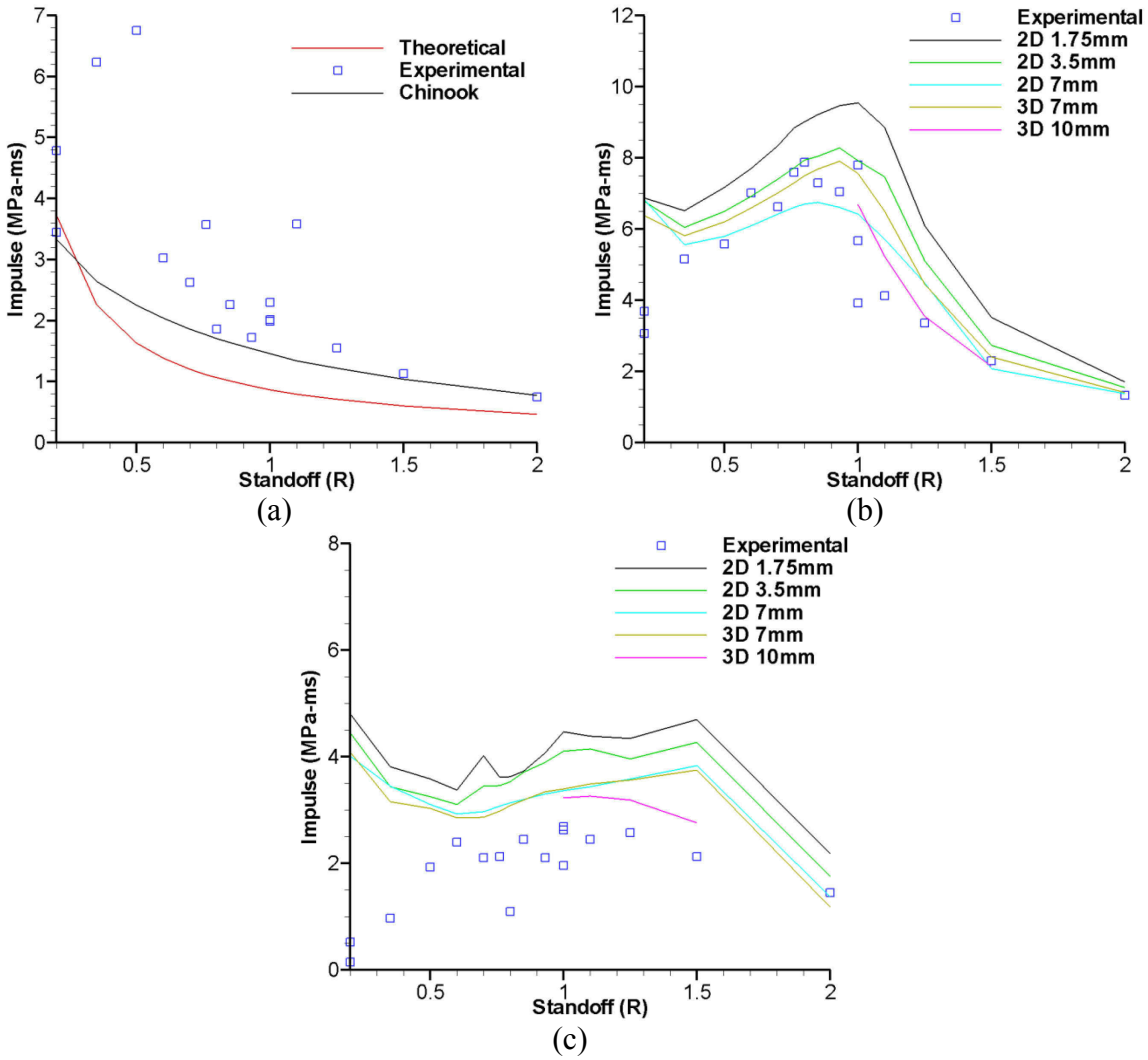

Figure 31: Comparison of the impulse increase as a function of the standoff for the 5 mm gauge location (a) Shock, (b) first bubble collapse, (c) second bubble collapse

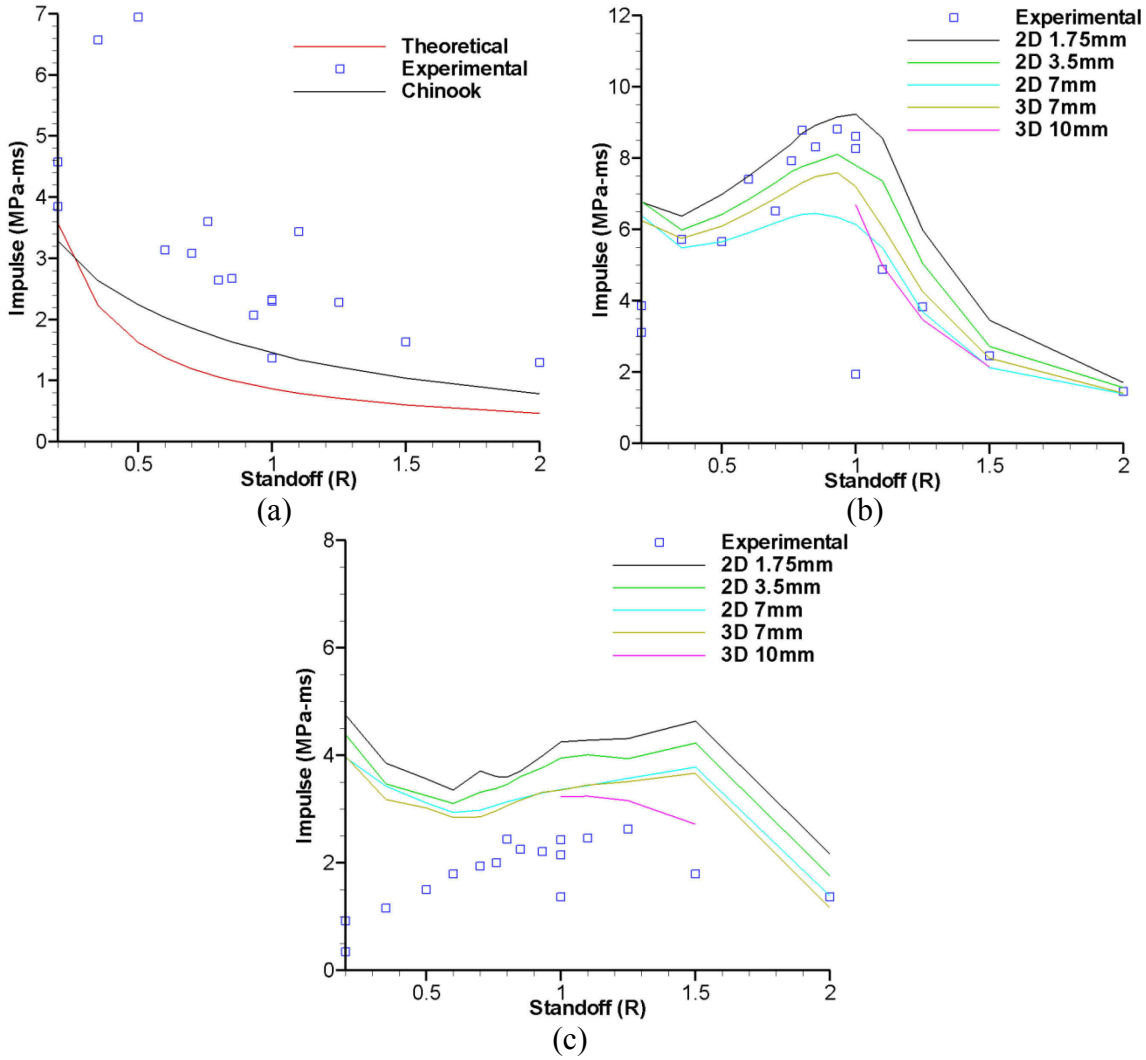

Figure 32: Comparison of the impulse increase as a function of the standoff for the 10 mm gauge location (a) Shock, (b) first bubble collapse, (c) second bubble collapse

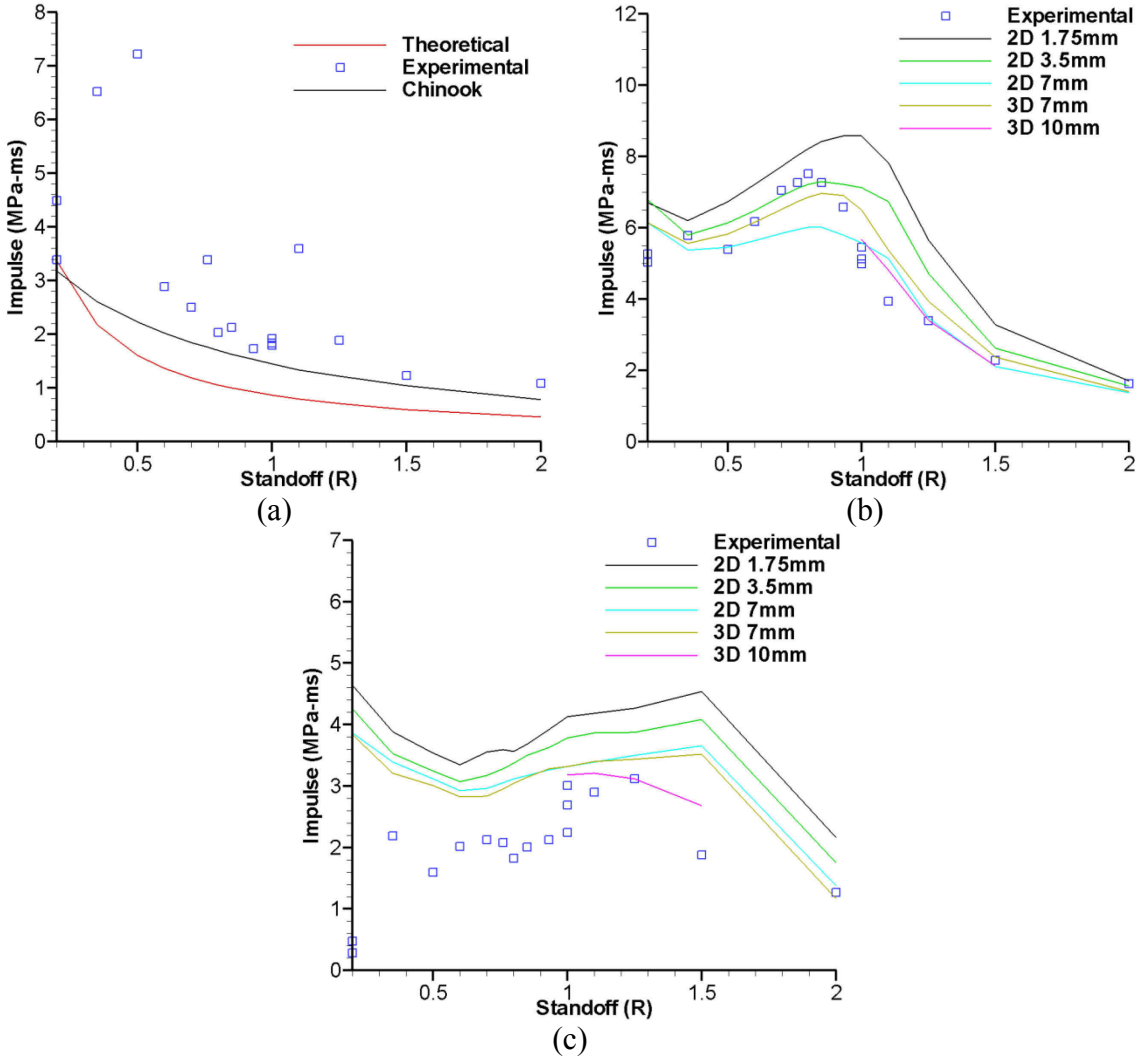

Figure 33: Comparison of the impulse increase as a function of the standoff for the 15 mm gauge location (a) Shock, (b) first bubble collapse, (c) second bubble collapse

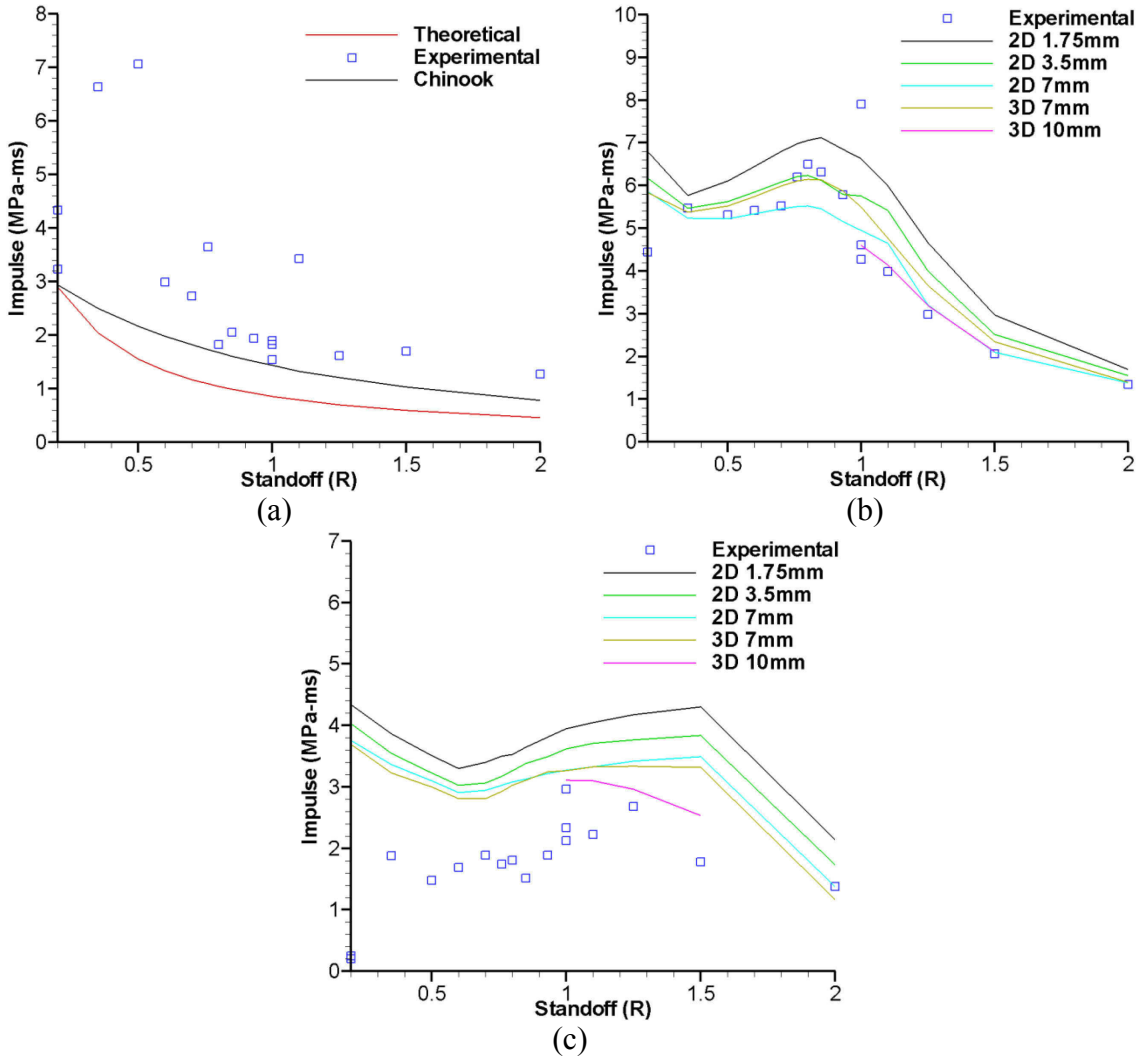

Figure 34: Comparison of the impulse increase as a function of the standoff for the 25 mm gauge location (a) Shock, (b) first bubble collapse, (c) second bubble collapse

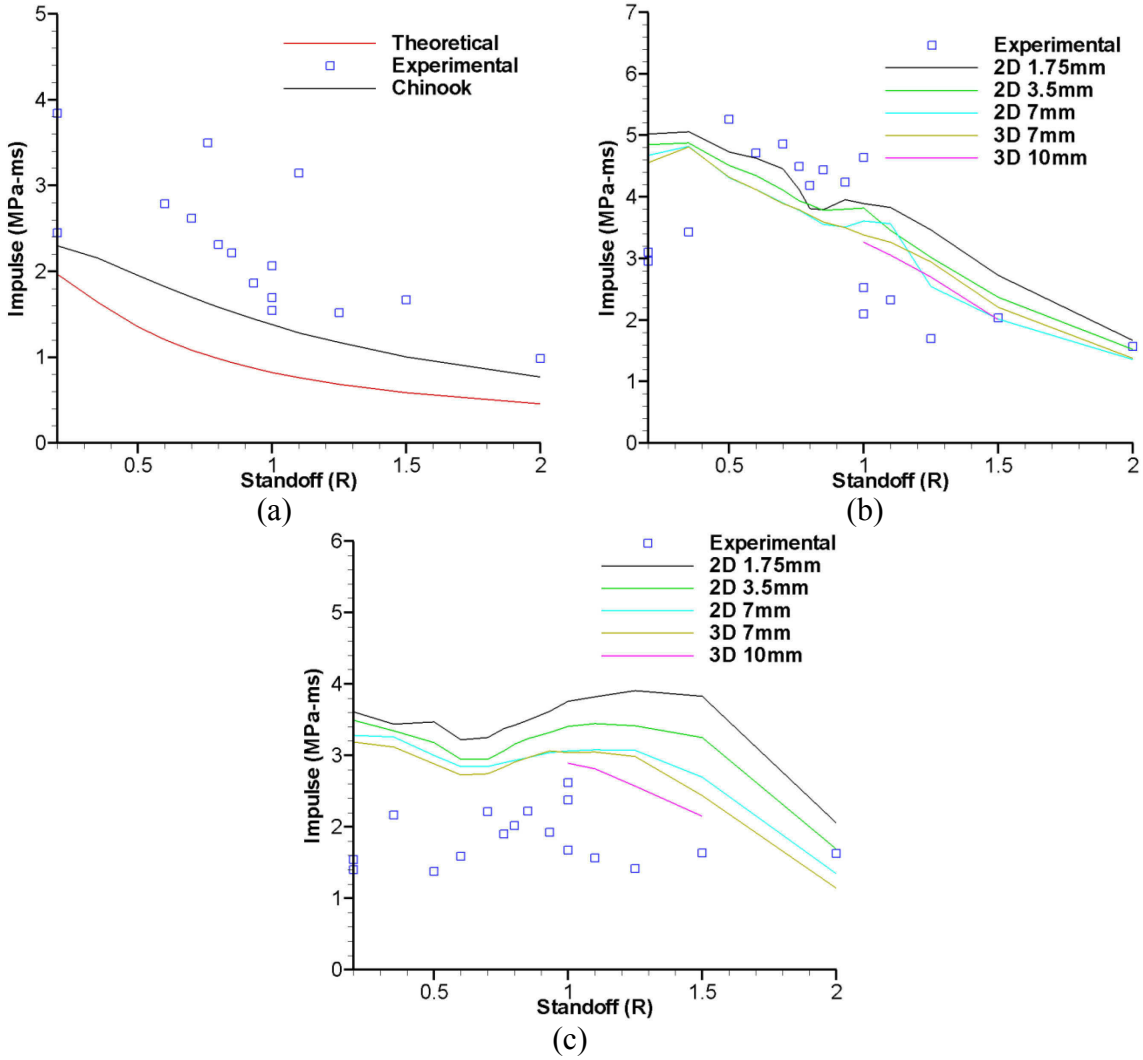

Figure 35: Comparison of the impulse increase as a function of the standoff for the 50 mm gauge location (a) Shock, (b) first bubble collapse, (c) second bubble collapse

List of symbols/abbreviations/acronyms/initialisms

CFD	Computational fluid dynamics
C4	Composition 4 explosive
D	Depth of charge detonation
DND	Department of National Defence
DRDC	Defence Research & Development Canada
DRDKIM	Director Research and Development Knowledge and Information Management
EOS	Equation of state
ft	Feet
I	Shockwave impulse
JWL	Jones-Wilkens-Lee equation of state
K_i	Similitude constants
Kg	Kilograms
lb	Pounds
m	Cycle counter in energy loss function (m=0,1,2,3,...)
MFP	Maritime force protection
ms	Milliseconds
P_{max}	Maximum shockwave pressure
R or R(t)	Gas bubble radius
R&D	Research & Development
t	Time
T_b	Gas bubble period
TNO	The Netherlands Organisation for Applied Scientific Research (Nederlandse Organisatie voor Toegepast Natuurwetenschappelijk Onderzoek)
UNDEX	Underwater explosion
V or V(t)	Gas bubble volume
V_o	Initial gas bubble volume
W	Charge weight
λ	Energy loss function
π	Numerical value of pi

θ	Shockwave decay constant

Distribution list

Document No.: DRDC Atlantic TM 2010-238

LIST PART 1: Internal Distribution by Centre

4 Author (2 paper copies, 2 CD's)
1 PM/MFPTDP (1 CD)
3 Library (2 CDs, 1 paper copy)
1 H/TD
1 H/WP Scientific Authority
2 GL/ NPSS (1 CD, 1 paper copy)

12 TOTAL LIST PART 1

LIST PART 2: External Distribution within Canada by DRDKIM

1 Library and Archives Canada (Attn: Military Archivist, Government Records Branch)

1 NDHQ/DRDKIM

1 Laura Ozimek
Directorate Science & Technology Maritime
Defence Research & Development Canada
305 Rideau, St.
Ottawa, ON K1A 0K2

1 Cdr D. Sims
National Defence Headquarters
DGMEPM/DMSS 2
555 Blvd de la Carriere
Hull, PQ K1A 0K2

1 Dr. Julian Lee
DRDC Suffield
P. O. Box 4000 Stn Main
Medicine Hat, AB T1A 8K6

5 TOTAL LIST PART 2

List Part 3: External Distribution outside Canada by DRDKIM

1 Adrian van der Made
Head Vulnerability & Construction
Defence Material Organisation
Van der Burchlaan 31
PO Box 90822 MPC 58A
2509 LV The Hague, The Netherlands

1 J.E. van Aanhold
TNO Built Environment and Geosciences
Van Mourik Broekmanweg 6
2628 XE Delft The Netherlands

1 J. M. Luyten
TNO Defence, Security and Safety
Lange Kleiweg 137
2288 GJ Rijswijk
The Netherlands

1 Niklas Alin
FOI - Swedish Defence Research Agency
Grindsjon Research Centre
SE-147 25 Tumba, Sweden

4 TOTAL LIST PART 3

21 TOTAL COPIES REQUIRED

DOCUMENT CONTROL DATA

(Security classification of title, body of abstract and indexing annotation must be entered when the overall document is classified)

1. ORIGINATOR (The name and address of the organization preparing the document. Organizations for whom the document was prepared, e.g. Centre sponsoring a contractor's report, or tasking agency, are entered in section 8.)

Defence R&D Canada – Atlantic
9 Grove Street
P.O. Box 1012
Dartmouth, Nova Scotia B2Y 3Z7

2. SECURITY CLASSIFICATION (Overall security classification of the document including special warning terms if applicable.)

UNCLASSIFIED

3. TITLE (The complete document title as indicated on the title page. Its classification should be indicated by the appropriate abbreviation (S, C or U) in parentheses after the title.)

Modeling Gas Bubble Behaviour and Loading on a Rigid Target due to Close-Proximity Underwater Explosions: Comparison to Tests Conducted at DRDC Suffield

4. AUTHORS (last name, followed by initials – ranks, titles, etc. not to be used)

Mark Riley

5. DATE OF PUBLICATION (Month and year of publication of document.)

November 2010

6a. NO. OF PAGES (Total containing information, including Annexes, Appendices, etc.)

74

6b. NO. OF REFS (Total cited in document.)

9

7. DESCRIPTIVE NOTES (The category of the document, e.g. technical report, technical note or memorandum. If appropriate, enter the type of report, e.g. interim, progress, summary, annual or final. Give the inclusive dates when a specific reporting period is covered.)

Technical Memorandum

8. SPONSORING ACTIVITY (The name of the department project office or laboratory sponsoring the research and development – include address.)

Defence R&D Canada – Atlantic
9 Grove Street
P.O. Box 1012
Dartmouth, Nova Scotia B2Y 3Z7

9a. PROJECT OR GRANT NO. (If appropriate, the applicable research and development project or grant number under which the document was written. Please specify whether project or grant.)

9b. CONTRACT NO. (If appropriate, the applicable number under which the document was written.)

10a. ORIGINATOR'S DOCUMENT NUMBER (The official document number by which the document is identified by the originating activity. This number must be unique to this document.)

DRDC Atlantic TM 2010-238

10b. OTHER DOCUMENT NO(s). (Any other numbers which may be assigned this document either by the originator or by the sponsor.)

11. DOCUMENT AVAILABILITY (Any limitations on further dissemination of the document, other than those imposed by security classification.)

12. DOCUMENT ANNOUNCEMENT (Any limitation to the bibliographic announcement of this document. This will normally correspond to the Document Availability (11). However, where further distribution (beyond the audience specified in (11) is possible, a wider announcement audience may be selected.))

Unlimited

13. ABSTRACT (A brief and factual summary of the document. It may also appear elsewhere in the body of the document itself. It is highly desirable that the abstract of classified documents be unclassified. Each paragraph of the abstract shall begin with an indication of the security classification of the information in the paragraph (unless the document itself is unclassified) represented as (S), (C), (R), or (U). It is not necessary to include here abstracts in both official languages unless the text is bilingual.)

This study describes recent simulation results for underwater explosions in close-proximity to a rigid target. Simulations were performed using Chinook, an Eulerian computational fluid dynamics (CFD) code. Predicted fluid pressures, impulse loading on the target, gas bubble size and bubble collapse times are compared with measurements taken from a series of experiments and compared to empirical models. The experiments, which were conducted at DRDC Suffield as part of the Force Protection TDP in 2008, involved 1.1 g detonator charges and 40 g C4 charges detonated at standoff distances ranging from 0.2 up to 2.0 times the free-field bubble radius from a rigid target. At these ranges of standoff distance, both the shock wave and gas bubble make significant contributions to the loading on the target surface.

The simulations of the rigid target tests primarily focused on the modelling of gas bubble collapse and water jetting behaviour. Both two-dimensional and three-dimensional simulations were performed. Chinook was found to qualitatively predict the general trends correctly, however quantitative gaps still exist. From the high speed experimental videos and the animation of the numerical simulations it was found that the maximum impulse due to a bubble collapse occurs for the largest standoff in which the bubble contacts the target before collapse. The results were found to be very mesh dependent, and refining the mesh did not always produce better agreement with experiments. This was observed most often in the bubble collapse impulse loading. The two-dimensional approach provided a good initial understanding of the physical behaviour for a limited computational effort, and produced better bubble periods when compared to experimental data. The three-dimensional simulations were found to produce improved impulse predictions for the rigid targets.

La présente étude décrit des résultats d'explosions sous-marines près d'une cible rigide simulées récemment. Les simulations ont été effectuées à l'aide de Chinook, un logiciel qui utilise la dynamique numérique des fluides et un résolveur à intervalles de temps explicites (méthode Euler). Les pressions de liquide prévues, la pression exercée sur la cible par l'impulsion, la taille des bulles de gaz et les temps d'effondrement des bulles sont comparés aux mesures tirées d'une série d'expériences et aux modèles empiriques. Les expériences, qui ont été réalisées à RDDC Suffield dans le cadre du projet de démonstration de technologies de protection de la Force maritime en 2008, impliquaient des charges à détonateur de 1,1 g et des charges de C4 de 40 g que l'on a fait exploser à une distance de sécurité, variant entre 0,2 et 2,0 fois le rayon de bulle de type champ libre, d'une cible rigide. À cette distance de sécurité, l'onde de choc et la bulle de gaz contribuent de façon significative à la pression exercée à la surface de la cible.

Les simulations des essais sur cible rigide se concentraient principalement sur la modélisation de l'effondrement des bulles de gaz et sur la formation des jets d'eau. Des simulations en deux dimensions et des simulations en trois dimensions ont été effectuées. On a découvert que le Chinook prédit de façon qualitative les tendances générales correctement bien qu'il y ait encore des failles au niveau quantitatif. À partir des vidéos expérimentaux à haute vitesse et de l'animation des simulations numériques, on a découvert que l'impulsion maximale due à l'effondrement d'une bulle se produit pour la plus importante distance dans laquelle la bulle

touche à la cible avant effondrement. On a découvert que les résultats dépendaient beaucoup du maillage; de plus, le fait de raffiner le maillage ne produisait pas toujours une plus grande conformité aux résultats expérimentaux. Cela a été observé la plupart du temps dans la pression d'impulsion d'effondrement de bulle. L'approche à deux dimensions a fourni une bonne compréhension initiale du comportement physique contre un effort d'analyse limité, et a produit de meilleures périodes de bulle que les données expérimentales. On a découvert que les simulations en trois dimensions produisent des prédictions d'impulsion améliorées pour les cibles rigides.

14. KEYWORDS, DESCRIPTORS or IDENTIFIERS (Technically meaningful terms or short phrases that characterize a document and could be helpful in cataloguing the document. They should be selected so that no security classification is required. Identifiers, such as equipment model designation, trade name, military project code name, geographic location may also be included. If possible keywords should be selected from a published thesaurus, e.g. Thesaurus of Engineering and Scientific Terms (TEST) and that thesaurus identified. If it is not possible to select indexing terms which are Unclassified, the classification of each should be indicated as with the title.)

UNDEX, close-proximity, Chinook simulations, experiments, rigid target, bubble collapse, bubble jetting

This page intentionally left blank.

This page intentionally left blank.

Defence R&D Canada

Canada's leader in defence
and National Security
Science and Technology

R & D pour la défense Canada

Chef de file au Canada en matière
de science et de technologie pour
la défense et la sécurité nationale

www.drdc-rddc.gc.ca